Plutonium oxide melt structure and covalency

Stephen K. Wilke, Chris J. Benmore, Oliver L. G. Alderman, Ganesh Sivaraman, Matthew D. Ruehl, Krista L. Hawthorne, Anthony Tamalonis, David A. Andersson, Mark A. Williamson & Richard Weber

Published version information

Citation: Wilke, S.K., Benmore, C.J., Alderman, O.L.G. et al. Plutonium oxide melt structure and covalency. Nat. Mater. 23, 884–889 (2024).

DOI: https://doi.org/10.1038/s41563-024-01883-3

Plutonium oxide melt structure and covalency

Stephen K. Wilke[1,2,*], Chris J. Benmore[2], Oliver L. G. Alderman[3], Ganesh Sivaraman[4], Matthew D. Ruehl[5], Krista L. Hawthorne[5], Anthony Tamalonis[6], David A. Andersson[7], Mark A. Williamson[5], Richard Weber[1,2]

[1] *Materials Development, Inc.; Evanston, IL 60202, USA.*

[2] *X-Ray Science Division, Advanced Photon Source, Argonne National Laboratory, Lemont, IL 60439, USA*

[3] *ISIS Neutron & Muon Source, Rutherford Appleton Laboratory, Chilton, Didcot, Oxon OX11 0QX, U.K.*

[4] *Department of Chemical & Biomolecular Engineering, University of Illinois at Urbana-Champaign, Urbana, IL 61801, USA*

[5] *Chemical and Fuel Cycle Technologies Division, Argonne National Laboratory, Lemont, IL 60439, USA*

[6] *Tamalonis Technologies, Highland Park, IL 60035, USA*

[7] *Materials Science and Technology Division, Los Alamos National Laboratory, Los Alamos, NM 87545, USA*

* *Corresponding author, email: swilke@matsdev.com*

Advances in nuclear power reactors include the use of mixed oxide fuel, containing uranium and plutonium oxides. High-temperature behavior and structure of PuO_{2-x} above 1800 K remain largely unexplored, and these conditions must be considered for reactor

design and planning mitigation of severe accidents. Herein, we measure the atomic structure of PuO_{2-x} through the melting transition up to 3000 ± 50 K using X-ray scattering of aerodynamically levitated and laser beam heated samples, with O/Pu ranging 1.57 to 1.76. Liquid structural models consistent with the X-ray data are developed using machine-learned interatomic potentials and density functional theory. Molten $PuO_{1.76}$ contains some degree of covalent Pu-O bonding, signaled by degeneracy of Pu 5*f* and O 2*p* orbitals. The liquid is isomorphous with molten $CeO_{1.75}$, demonstrating the latter as a nonradioactive, nontoxic, structural surrogate when differences in oxidation potential of Pu and Ce are accounted for. These characterizations provide essential constraints for modeling pertinent to reactor safety design.

Nuclear energy is one of several sources that will play a key role in decarbonizing electric power generation, but longstanding challenges associated with waste management hinder its widespread use[1]. One promising advancement is the use of mixed oxide fuels (MOX) containing U, Pu, and other actinide oxides in both Gen-III and Gen-IV reactors[2]. MOX fuel can make use of Pu and other actinides recycled from the used fuel of current Gen-III reactors, improving energy utilization, reducing the amount of waste disposed in a geologic repository, and decreasing the time required for Gen-III waste isolation to 300 instead of 300,000 years[3]. MOX fuel can also provide a pathway for repurposing excess weapons-grade Pu[4,5].

Reactor design for MOX fuel relies heavily on thermochemical models that are based on experimental measurements. Yet, experimental data on thermophysical properties and chemistry of plutonium oxides are scarce above 1800 K[6,7] because of challenges working at high temperature, such as sample contamination from reactions with most crucible materials, in

addition to safety hazards of radioactivity and toxicity. PuO_2 can lose oxygen to form PuO_{2-x} above ~1000 K, with the O/Pu ratio dependent on temperature and oxygen chemical potential. No structure data are available for Pu-O solids above 1773 K[8,9]. There are no reported experimental data for the liquid[6] except for melting point, T_m, which recently was reassessed to be 300 K higher than decades' of past research had suggested[10]. Only two molecular dynamics studies have included the liquid, limited to stoichiometric PuO_2[11,12]. The paucity of experimental information on high-temperature and melting behavior of Pu-O must be addressed to enable reactor and safety design for deployment of MOX-fueled reactors, including under hypothetical accident conditions. Herein, we use aerodynamic levitation, laser beam heating, and X-ray total scattering to measure the structure of PuO_{2-x} up to 3000 ± 50 K under various oxygen partial pressures. We demonstrate, by analogous measurements on cerium oxides, that its melt is structurally similar to CeO_{2-x}, a commonly used nonradioactive surrogate for PuO_{2-x}.

For high-temperature structure measurements, high-energy synchrotron X-ray diffraction was performed with aerodynamically levitated and laser beam heated PuO_{2-x} spheroids ~2 mm in diameter[13]. The levitation technique enables high-temperature studies without risking sample contamination from container interactions. As shown in Fig. 1a, diffraction was measured by transmission of X-rays through the top of the sample, where the heating laser and an optical pyrometer were aligned. Samples initially appeared matte grey and after heating were shiny black (Fig. 1b). Samples were heated and melted under 1% O_2 (Ar balance), Ar, or 5% CO (Ar balance) gases to access different O/Pu ratios (Fig. 1c). The relationship between fluorite PuO_{2-x} (f-PuO_{2-x}) composition and oxygen partial pressure, previously determined from experimental data up to 2050 K[14], was extrapolated to the solidus and yielded melt compositions of $PuO_{1.76}$, $PuO_{1.69}$, and $PuO_{1.57}$ for the gases used here. For example, the heating trajectory for a sample

heated in 5% CO is shown in Fig. 1c with pink shading. (Compositional uncertainty in O/Pu is ca. ± 0.03, as discussed in the Supplementary Information (SI) along with a comparison of different published oxidation models.) Heating was attempted with pure O_2 gas, but PuO_{2-x} volatilized severely above 2300 K and full melting was not achieved (Fig. 1c, inset); further heating in O_2 was aborted to avoid rapid sample loss by volatilization. This raises considerations pertinent to accidental melting of MOX fuels, which upon contacting air may release vapors containing plutonium oxides.

X-ray diffraction data were reduced and corrected to obtain the total X-ray structure factor, *S(Q)*, where Q is the magnitude of the scattering vector, $Q = 4\pi \sin(\theta)/\lambda$, 2θ is the scattering angle, and λ is the X-ray wavelength[15]. Figure 2a shows the PuO_{2-x} structure factors during heating under 5% CO (Ar balance) at temperatures shown by the red markers in Fig. 1c. The sample was initially a mixture of *f*-PuO_{2-x}, cubic α-Pu_2O_3, and hexagonal β-Pu_2O_3 with a mean composition of $PuO_{1.81}$. Upon heating, it transformed entirely to *f*-PuO_{2-x} between 1350 and 1530 K, consistent with the phase diagram. Diffuse scattering appeared above 1930 K, and upon further heating the Bragg peak intensities decreased while diffuse scattering increased, until the sample became fully molten between 2630 and 2730 K. Over this wide temperature range (2140-2630 K), the scattering is consistent with a mixture of mostly liquid and a small amount of *f*-PuO_{2-x}, which results from temperature gradients in the sample due to the focused spot of the heating laser and stochastic sample motions during the melting process. Temperature gradients result in uncertainty for levitated solids of typically ± 150 K[16] until they are fully molten (see SI). Sample motion can occur for solids just prior and during partial melting, during which time the sample is not stably aligned with the heating laser and X-ray beam. In the context of Fig. 1c, the heating trajectory shaded in pink is thus the general pathway, though different regions of the

sample were at varying locations along the trajectory, resulting in the observed solid/liquid mixture. For these reasons, compositional and lattice parameter calculations over 2140-2630 K should be treated with caution, and as such these data markers are shaded half-full in Figs. 1c and 2b. (Once fully molten, levitation was stable, and temperature uncertainty is typically ± 50 K.) The point of full melting (above 2630 K) is ~200 K higher than T_m = 2410 K according to the phase diagram, but the thermal gradients in partially-solid samples make any critical comparison of T_m difficult.

Figure 2b shows the change in atomic number density during heating under 5% CO (Ar balance). The *f*-PuO_{2-x} phase's density decreased approximately linearly from 300 to 1800 K and then asymptotically approached 0.0592 atoms $Å^{-3}$ as temperature approached T_m = 2410 K. These density changes occurred due to thermal expansion of the lattice (Fig. 2b, black line, from dilatometry[17]) and decreasing O/Pu ratio, corresponding to chemical expansion of the lattice (Fig. 2b, colored open squares, from X-ray diffraction[18]). The sample compositions estimated from equilibrium with the gas (Fig. 2b, see colors of triangle markers) have O/Pu ratios 0.03-0.06 higher than those predicted by extrapolation of prior chemical expansion data. The pink shaded trajectory in Fig. 1c illustrates this compositional uncertainty, which lies within the gas pO_2 uncertainty. As shown in Fig. 1c, upon reaching the solidus at a composition of $PuO_{1.65}$, the material melts isothermally while following the oxygen isobar to a composition of $PuO_{1.57}$. The arrest in lattice expansion (and density) upon approaching T_m is consistent with previous observations at much lower temperature (1273 K) that incremental chemical expansion diminishes as O/Pu decreases and approaches 1.61[18]. This behavior is likely because the O vacancies responsible for chemical expansion reach a high concentration and associate into

clusters[19]. Upon melting, $PuO_{1.57}$ density decreases to 0.0559 atoms Å^{-3} (9.65 g cm^{-3}), ~6% less than molten UO_2 (0.0593 atoms Å^{-3})[20] and consistent with the lower O content in $PuO_{1.57}$.

Figure 3a provides the X-ray structure factor for molten $PuO_{1.76}$ at 3000 K. The first principal peak position, Q_1, decreases by 0.014 Å^{-1} as O/Pu increases from 1.57 to 1.76. This small Q_1 variation suggests minimal redox-induced differences in Pu-Pu periodicity and the Pu-O polyhedral units that comprise the melt structure. In contrast, molten UO_{2-x} composition varies much more than PuO_{2-x} over this pO_2 range[21]: O/U is likely less than 1 in 5% CO (Ar balance) and increases to 1.93 under Ar, but Q_1 increases only 0.03 Å^{-1}. This suggests that Q_1 is only weakly sensitive to redox-induced structural changes, and/or that cation-cation periodicity changes are subtle.

Figure 3b shows the X-ray weighted total pair distribution function (PDF), $T(r)$, for $PuO_{1.76}$, obtained from the sine Fourier transform of the structure factor[15]. The PDF's first peak is too broad and asymmetric to be fitted well with a single Gaussian distribution (Extended Data Fig. 1a). The necessity of fitting with two distinct Pu-O distributions motivated the use of separate Pu(III) and Pu(IV) species in an atomic structure model, created using empirical potential structure refinement (EPSR)[22]. The EPSR model agrees well with the X-ray scattering data (Fig. 3a-c). The model's atomic partial pair correlations (Fig. 3b) show overlapping Pu(III)-O and Pu(IV)-O distributions with mean bond lengths of 2.55 and 2.29 Å and mean coordination numbers of 6.0(5) and 5.8(5). The relatively shorter mean bond length for Pu(IV)-O is consistent with its larger charge, given the similar mean coordination numbers for both Pu(III)-O and Pu(IV)-O. The overall Pu-O mean coordination is 5.9(4), compared to n_{PuO} = 8 for *f*-PuO_2 and 6 for α-Pu_2O_3 (Fig. 3d). Using the average of the crystalline phases, since $PuO_{1.76}$ lies midway compositionally, the melt n_{PuO} is 5.9/7 = 84% of that in the crystal, which is similar to molten

UO_2: n_{UO} = 6.7, or 6.7/8 = 84% of the crystal[20]. The $PuO_{1.76}$ melt structure consists of Pu-O polyhedra with coordination ranging from 4 to 8, with preferential clustering of polyhedra with similar coordination (Fig. 3c). Polyhedra are connected by 65% corner-, 29% edge-, and 6% face-sharing.

A longstanding question in actinide chemistry is the extent to which 5*f* valence orbitals participate in covalent bonds[23]. If Pu-O bonding has different covalency than the lanthanides, this property could be exploited to improve chemical processing methods for used nuclear fuel that separate Pu from lanthanide fission products. Both solid and liquid UO_2 are mostly ionic, indicative of highly localized 5*f* electrons[20,24,25]. Density functional theory (DFT) calculations on the actinide dioxides ThO_2 through EsO_2 have revealed some covalency in the intermediate region of PuO_2 to CmO_2, evidenced by degeneracy between actinide 5*f* and O 2*p* orbitals beginning with PuO_2[25–27]. This trend in covalency has also been linked with the lower oxidation tendency of NpO_2 and PuO_2 compared to UO_2, which exhibits an energy gap between U 5*f* and O 2*p*[28]. However, X-ray absorption near edge structure and resonant inelastic X-ray scattering measurements on PuO_2 in solution have indicated that the 5*f* states in Pu are less active in the chemical bonding[29].

To investigate whether Pu-O covalency is present in the melts, another modeling approach was implemented since EPSR cannot provide information on electronic structure. A machine-learned Gaussian approximation potential[30] (GAP) was developed at the level of DFT+U calculations (including Coulomb potential) for PuO_{2-x} and then implemented in a molecular dynamics (MD) simulation[31]. (See SI for details.) In prior works, MD simulations based on empirical potentials have often been relied on for calculating properties such as density, enthalpy, specific heat, bulk modulus, and melting points[7,11,12] for compositionally complex phases in

185 nuclear fuels and under extreme conditions that are difficult to access experimentally. One major
186 limitation is developing MD potentials that can reproduce experimental data, and most MD
187 models are validated using only solid phase information due to the lack of liquid and high-
188 temperature experiments. Empirical potentials also have the limitation of only treating one cation
189 oxidation state, for example in prior MD modeling of molten UO_2[20].

190 The GAP-MD model here agrees well with the liquid structure X-ray measurement for
191 $PuO_{1.76}$ (Fig. 3a-b), illustrating why such measurements are crucial to validating the structural
192 models that are used to estimate material properties. The projected density of states (PDOS) was
193 calculated from the model and is shown in Fig. 3e. Below the highest occupied state, the
194 significant degeneracy between Pu 5*f* and O 2*p* orbitals suggest that some covalency is present in
195 the melt structure. This finding of covalency could be an important property that sets Pu-O apart
196 from the lanthanides. While similar to previous DFT+U results for crystalline PuO_2[25–27], this is
197 the first such model for hypostoichiometric PuO_{2-x} compositions and for the liquid state. The
198 GAP-MD approach is also an advancement in modeling the mixture of Pu(III) and Pu(IV)
199 oxidation states, which is a challenge for empirical MD potentials.

200 Cerium oxide, CeO_{2-x} (Extended Data Fig. 2), is often used as a surrogate material for
201 research on PuO_{2-x} to avoid radioactivity and toxicity hazards. Both Ce and Pu exist in 3+ and 4+
202 oxidation states, and their dioxides have similar redox activity and melting temperatures: CeO_2 at
203 3000 K (congruent, accessible only under high-pressure O_2)[32], and PuO_2 at 3017 K[10]. Surrogacy
204 of CeO_{2-x} for PuO_{2-x} has been demonstrated for powder processing and sintering of MOX fuel
205 pellets[33] and thermally induced gallium removal[34]. However, Ce(IV) is more easily reduced to
206 Ce(III) as compared with Pu, which has made it an inadequate analogue for studies of Pu
207 solubility in vitrified nuclear waste[35,36], chemical separation and purification processes including

PUREX and other aqueous technologies[37], and inorganic chemical synthesis[38]. In these cases, poor surrogacy arises from the larger Ce(III)/Ce(IV) ratio compared to Pu(III)/Pu(IV) for certain ranges of oxygen potential, though under highly oxidizing conditions the surrogacy is improved[39]. This motivates an evaluation of Ce surrogacy for Pu in the oxide melts.

Figure 4a shows the PDFs for $PuO_{1.76}$, melted under 1% O_2 (Ar balance) at 3000 K, and $CeO_{1.75}$, melted under pure O_2 at 2580 K. The PDFs are qualitatively similar, though the relative peak magnitudes naturally differ due to the materials' different X-ray weighting factors (Extended Data: Fig. 3 and Table 1), arising from the different numbers of core electrons on the two cations. With the weighting factors removed, the atomic partial pair correlations for metal-oxygen (MO), metal-metal (MM), and oxygen-oxygen (OO) are nearly identical for the two EPSR models. The Ce-O first coordination shell is slightly broader than Pu-O, though with similar mean coordination (6.1(4) vs. 5.9(4)). The distributions of M-O and O-M coordination environments are also similar (Fig. 4b-c). M-O coordination has a mode of 6 and approximately equal portions of MO_5 and MO_7. The M(III)-O pairs are slightly shifted to less 5-coordinate and more 7-coordinate, as compared to M(IV)-O pairs. The O-M coordination is mostly 3- and 4-coordinate with a variety of O-{M(III),M(IV)} local environments. Higher O-M coordination correlates with environments richer in M(III).

Bond angle distributions for O-M-O and M-O-M are nearly identical for $PuO_{1.76}$ and $CeO_{1.75}$ melts (Fig. 4d), both showing broad distributions indicative of distorted polyhedra with varying coordination. The O-M-O peaks near 80 and 170° likely represent the octahedral MO_6 species, which are more similar to the α-Pu_2O_3 crystalline phase than *f*-PuO_2. Statistics for shortest-path -M-O- rings[40] are also similar in the two melts (Fig. 4e). Modal ring size is 4 cations. Only 17% of atoms participate in rings with 5 cations, and almost no rings contain more than 5 cations.

This lack of larger rings matches other non-glass-forming oxide melts, such as HfO_2[41], in contrast to glass-forming systems like SiO_2 that contain substantial populations of 6- and 7-cation rings[40].

The similarity in X-ray PDFs and structural models for $PuO_{1.76}$ and $CeO_{1.75}$ indicate that cerium oxide is an excellent liquid structure analogue for plutonium oxide, once differences in redox activity are adjusted to obtain similar M(III)/M(IV) ratios. This suggests that Ce surrogacy for Pu could be improved in other applications such as nuclear waste vitrification, if oxidation potential differences can be judiciously corrected. The structural similarity of the melts is also consistent with their bonding character: like PuO_{2-x}, DFT calculations and X-ray absorption spectroscopy for crystalline *f*-CeO_2 have evidenced some covalent character via degeneracy of Ce 4*f* and O 2*p* orbitals[42].

Atomistic structural knowledge of molten plutonium oxide and its redox dependence provide useful experimental data to validate structural and thermochemical modeling for Pu-O, Pu-U-O, and other MOX fuels in the high-temperature range encompassing their melting points. Such modeling efforts remain a primary route for estimating thermophysical properties and material behavior in extreme operating conditions, which are necessary for engineering and safety design of advanced nuclear power reactors.

Acknowledgements. This work was supported by the U.S. Department of Energy (DOE) through grants DE-SC0018601 and DE-SC0015241 and the Argonne Laboratory Directed Research and Development program. X-ray diffraction measurements were made at Sector 6-ID-D of the Advanced Photon Source, a U.S. DOE Office of Science User Facility, operated by Argonne National Laboratory under Contract No. DE-AC02-06CH11357. The authors gratefully

254 acknowledge John Vacca, Lynn Soderholm, Wendy VanWingeren and Elizabeth Schmidt for
255 technical advice and safety management contributions that enabled the X-ray measurements,
256 Mark Schvaneveldt for assembling the sample chamber, Andrew Hebden for sample chamber
257 design considerations, and Steve Salbeck, Hadco Tool, LLC, for advice and fabrication of sample
258 handling, nozzle housing, and sample die components.
259

260 **Author contributions.** C.J.B., O.L.G.A., M.A.W., and R.W. conceived the idea for X-ray
261 diffraction measurements and developed the sample chamber with A.T. O.L.G.A. wrote the
262 proposal for X-ray beamtime. S.K.W., C.J.B., and R.W. conducted the X-ray measurements.
263 S.K.W. analyzed the X-ray data and performed the empirical potential structure refinements with
264 guidance from C.J.B., O.L.G.A., and R.W. G.S. developed the Gaussian approximation potential
265 from density functional theory calculations and performed molecular dynamics simulations,
266 under guidance of D.A.A. M.D.R. and K.L.H. prepared the PuO_2 samples and facilitated
267 radioactive sample handling under the guidance of M.A.W. S.K.W. prepared the manuscript
268 draft, with revisions contributed by all.
269

270 **Competing interests.** The authors declare no competing interests.
271

272 **Figure Captions**

273 **Fig. 1. Aerodynamic levitation and laser beam heating of PuO_{2-x} high-temperature solids**
274 **and melts. a,** Cross-section schematic of the sample on the levitation nozzle. **b,** Pictures of a
275 PuO_{2-x} pellet before (left) and after (right) melting under 5% CO (Ar balance). **c,** Pu-O phase
276 diagram[43] with oxygen gas partial pressure (pO_2) isobars (dashed colored curves)[14]. X-ray

scattering measurements were taken at the red triangle markers (no fill = solid; filled = liquid; half-filled = solid/liquid mixture). The redox trajectory for a sample heated in 5% CO (Ar balance) is shaded in pink. Representative error bars are shown for solid and liquid measurements, as discussed in the SI. The inset picture is a sample after heating under pure O_2 gas, which exhibited severe volatilization before reaching T_m.

Fig. 2. X-ray total scattering of high-temperature PuO_{2-x}. a, X-ray structure factors under 5% CO (Ar balance). **b,** Atomic number density measured for *f*-PuO_{2-x} and liquid (triangles), with markers' colors corresponding to the O/Pu ratio given by the pO_2 isobars in Fig. 1c. Triangle markers are unfilled for solid samples, filled for liquid samples, and half-filled for solid/liquid mixtures. Representative error bars are shown for solid and liquid measurements. Density changes due to thermal expansion (black line)[17] and chemical reduction (colored squares)[18] are shown up to the maximum temperatures previously reported.

Fig. 3. Structure of molten $PuO_{1.76}$. a, X-ray structure factor and comparison to models from empirical potential structure refinement (EPSR) and Gaussian approximation potential[30] driven molecular dynamics (GAP-MD). Inset: position of the first principal peak for liquids of differing compositions. **b,** Total pair distribution function (PDF) with comparison to models and the EPSR X-ray weighted atomic partial pair correlations (Q_{max} = 17.4 $Å^{-1}$). The Pu-O partial comprises separate contributions for Pu(III)-O and Pu(IV)-O, shown with dashed lines up to their cutoff distance used for structure calculations (r = 3.21 Å, corresponding to the minimum in the total Pu-O partial). **c,** Atomic structure snapshot from the EPSR model. **d,** Mean bond distances and coordination numbers obtained from Gaussian peak fitting and EPSR, compared with the crystal

phases. **e,** Averaged projected density of states (DOS) for Pu 5*f* and O 2*p* electrons. The highest occupied state is set to zero, and spin-up and spin-down components are displayed as positive and negative values.

Fig. 4. Structural surrogacy of CeO_{2-x} for PuO_{2-x} melts. a, X-ray weighted PDFs, *G(r)*, for $PuO_{1.76}$ at 3000 K and $CeO_{1.75}$ at 2580 K, compared with their EPSR models (Q_{max} = 11.9 Å^{-1}). Unweighted atomic partial pair PDFs, $g_{ij}(r)$, from EPSR for metal-oxygen (MO), metal-metal (MM), and oxygen-oxygen (OO) pairs in the two melts. **b,** Distribution of M-O coordination numbers, separated by oxidation state into M(III)-O and M(IV)-O components. **c,** Distribution of O-M coordination numbers. Increasing darkness of the color bars represents O local environments with increasing number of M(IV) neighbors. **d,** Distributions for O-M-O and M-O-M bond angles, after division by the *sin(θ)* dependence for a random angle distribution, compared with the crystalline phases for *f*-PuO_2 and α-Pu_2O_3. **e,** Frequency of shortest-path -M-O- rings, R_C, and the fraction of atoms participating in rings of a given size, P_N. Fractions do not sum to unity since a given atom can participate in multiple rings.

Extended Data Fig. 1. Fitting of Gaussian distributions to the total PDF for molten $PuO_{1.76}$. **a,** Fitting a single PuO distribution to the leading edge of the first peak, and a single PuPu distribution to the leading edge of the second peak. **b,** Optimized peak fitting for all pair correlations, guided by the bond distances and coordinations anticipated from *f*-PuO_2 and α-Pu_2O_3 crystal structures.

Extended Data Fig. 2. Ce-O phase diagram. Colored markers show oxygen gas partial pressure (pO_2) isobars[32]. The redox trajectory for a sample heated under pure O_2 is shaded in pink.

Extended Data Fig. 3. Examples of sample temperature during levitation and laser beam heating. a, Emissivity-corrected temperature measurements (10 Hz acquisition) from the optical pyrometer for PuO_{2-x} solid heated under 5% CO (Ar balance). Laser power was increased incrementally, interspersed with X-ray diffraction measurements taken while the sample was held isothermally. **b,** Zoomed-in view of a single isotherm from (**a**). For the time period 364-416 s, the temperature mean was 2140 K with a standard deviation of 71 K. **c,** Temperature of molten $PuO_{1.57}$ during a different heating run than (**a-b**). X-ray measurements were analyzed for the time period 105-110 s, which had a temperature mean of 2730 K and a standard deviation of 2 K.

Extended Data Fig. 4. Faber-Ziman X-ray weighting factors. a, $PuO_{1.76}$. **b,** $CeO_{1.75}$. From Eqn. 2.

Extended Data Fig. 5. X-ray diffraction and Rietveld refinements for selected crystalline samples. a, Initial Pu-O material before heating. **b,** Pure *f*-PuO_2 after heating under O_2. The observed X-ray diffraction patterns (green curves) and calculated Rietveld refinement models (orange curves) are compared against the Bragg reflections for *f*-PuO_2, α-Pu_2O_3, and β-Pu_2O_3 (blue, teal, and red vertical ticks). The black curves show the differences between the X-ray data and refinement models, divided by the estimated standard uncertainties.

Extended Data Fig. 6. Fitting of a Lorentzian function to the structure factor's first principal peak, for molten $PuO_{1.76}$. The fit[44] includes the Lorentzian contribution mirrored across $Q = 0$ Å^{-1} and is constrained[15] to $S(0) = 1 - \langle f(0)^2 \rangle / \langle f(0) \rangle^2$ = -1.113. The X-ray diffraction data were extrapolated to $Q = 0$ using this Lorentzian fit, prior to the Fourier transform to obtain the PDFs (Eqn. 3-4).

Extended Data Fig. 7. Effect of top hat convolution on X-ray data. Comparison of the (a) X-ray structure factor and (b) total PDF for molten $PuO_{1.76}$, processed with and without the top hat convolution[45] in GudrunX. For this comparison, Q_{max} = 11.9 Å^{-1} was used for both structure factors to avoid large truncation oscillations in the PDF without top hat.

1. Intergovernmental Panel on Climate Change. *Climate Change 2022: Mitigation of Climate Change*. (2022)
2. Abram, T. & Ion, S. Generation-IV nuclear power: A review of the state of the science. *Energy Policy* **36**, 4323–4330 (2008).
3. Chang, Y. Il *et al.* Conceptual Design of a Pilot-Scale Pyroprocessing Facility. *Nucl. Technol.* **205**, 708–726 (2019).
4. Carbajo, J. J., Yoder, G. L., Popov, S. G. & Ivanov, V. K. A review of the thermophysical properties of MOX and UO2 fuels. *J. Nucl. Mater.* **299**, 181–198 (2001).
5. IAEA. *Status and Advances in MOX Fuel Technology*. (2003).
6. Fouquet-Métivier, P. *et al.* Investigation of the solid/liquid phase transitions in the U–Pu–O system. *Calphad* **80**, 102523 (2023).
7. Guéneau, C., Chartier, A., Fossati, P., Van Brutzel, L. & Martin, P. Thermodynamic and

Thermophysical Properties of the Actinide Oxides. in *Comprehensive Nuclear Materials 2nd edition* 111–154 (Elsevier, 2020).

8. Vauchy, R., Joly, A. & Valot, C. Lattice thermal expansion of Pu1−yAmyO2-x plutonium–americium mixed oxides. *J. Appl. Crystallogr.* **50**, 1782–1790 (2017).

9. Boivineau, J. C. Etude par rayons x du diagramme plutonium-oxygene de la temperature ambiante jusqu'a 1100°c. *J. Nucl. Mater.* **60**, 31–38 (1976).

10. De Bruycker, F. *et al.* Reassessing the melting temperature of PuO2. *Mater. Today* **13**, 52–55 (2010).

11. Ghosh, P. S. *et al.* Melting behavior of (Th,U)O2 and (Th,Pu)O2 mixed oxides. *J. Nucl. Mater.* **479**, 112–122 (2016).

12. Cooper, M. W. D., Murphy, S. T., Rushton, M. J. D. & Grimes, R. W. Thermophysical properties and oxygen transport in the (Ux,Pu1-x)O2 lattice. *J. Nucl. Mater.* **461**, 206–214 (2015).

13. Weber, J. K. R. *et al.* Aerodynamic levitator for in situ x-ray structure measurements on high temperature and molten nuclear fuel materials. *Rev. Sci. Instrum.* **87**, 073902 (2016).

14. Besmann, T. M. & Lindemer, T. B. Chemical thermodynamic representations of <PuO2-x> and <U1-zPuzOw>. *J. Nucl. Mater.* **130**, 489–504 (1985).

15. Benmore, C. J. X-Ray Diffraction from Glass. in *Modern Glass Characterization* 241–270 (John Wiley & Sons, Inc., 2015).

16. McCormack, S. J., Tamalonis, A., Weber, R. J. K. & Kriven, W. M. Temperature gradients for thermophysical and thermochemical property measurements to 3000 °C for an aerodynamically levitated spheroid. *Rev. Sci. Instrum.* **90**, 15109 (2019).

17. Uchida, T., Sunaoshi, T., Konashi, K. & Kato, M. Thermal expansion of PuO2. *J. Nucl.*

Mater. **452**, 281–284 (2014).

18. Gardner, E. R., Markin, T. L. & Street, R. S. The plutonium-oxygen phase diagram. *J. Inorg. Nucl. Chem.* **27**, 541–551 (1965).

19. Kato, M., Nakamura, H., Watanabe, M., Matsumoto, T. & Machida, M. Defect chemistry and basic properties of non-stoichiometric PuO2. *Defect Diffus. Forum* **375**, 57–70 (2017).

20. Skinner, L. B. *et al.* Molten uranium dioxide structure and dynamics. *Science* **346**, 984–987 (2014).

21. Alderman, O. L. G. *et al.* The structure of liquid UO2−x in reducing gas atmospheres. *Appl. Phys. Lett.* **110**, 081904 (2017).

22. Soper, A. K. Empirical potential Monte Carlo simulation of fluid structure. *Chem. Phys.* **202**, 295–306 (1996).

23. Neidig, M. L., Clark, D. L. & Martin, R. L. Covalency in f-element complexes. *Coord. Chem. Rev.* **257**, 394–406 (2013).

24. Desgranges, L., Baldinozzi, G., Fischer, H. E. & Lander, G. H. Temperature-dependent anisotropy in the bond lengths of UO2 as a result of phonon-induced atomic correlations. *J. Phys. Condens. Matter* **35**, 10LT01 (2023).

25. Wen, X. D., Martin, R. L., Henderson, T. M. & Scuseria, G. E. Density functional theory studies of the electronic structure of solid state actinide oxides. *Chem. Rev.* **113**, 1063–1096 (2013).

26. Prodan, I. D., Scuseria, G. E. & Martin, R. L. Covalency in the actinide dioxides: Systematic study of the electronic properties using screened hybrid density functional theory. *Phys. Rev. B* **76**, 033101 (2007).

27. Yang, Y. & Zhang, P. Chemical bonds and vibrational properties of ordered (U, Np, Pu) mixed oxides. *J. Appl. Phys.* **113**, 013501 (2013).

28. Andersson, D. A., Lezama, J., Uberuaga, B. P., Deo, C. & Conradson, S. D. Cooperativity among defect sites in AO2+x and A4O9 (A=U,Np,Pu): Density functional calculations. *Phys. Rev. B* **79**, 024110 (2009).

29. Vitova, T. *et al.* The role of the 5f valence orbitals of early actinides in chemical bonding. *Nat. Commun.* **8**, 16053 (2017).

30. Bartók, A. P., Payne, M. C., Kondor, R. & Csányi, G. Gaussian Approximation Potentials: The Accuracy of Quantum Mechanics, without the Electrons. *Phys. Rev. Lett.* **104**, 136403 (2010).

31. Sivaraman, G. *et al.* Experimentally Driven Automated Machine-Learned Interatomic Potential for a Refractory Oxide. *Phys. Rev. Lett.* **126**, 156002 (2021).

32. Zinkevich, M., Djurovic, D. & Aldinger, F. Thermodynamic modelling of the cerium-oxygen system. *Solid State Ionics* **177**, 989–1001 (2006).

33. Kim, H. S. *et al.* Applicability of CeO2 as a surrogate for PuO2 in a MOX fuel development. *J. Nucl. Mater.* **378**, 98–104 (2008).

34. Kolman, D. G., Park, Y., Stan, M., Hanrahan, R. J. & Butt, D. P. An assessment of the validity of cerium oxide as a surrogate for plutonium oxide gallium removal studies. *LA-UR-99-0491* (1999).

35. Darab, J. G. *et al.* Redox chemistry of plutonium and plutonium surrogates in vitrified nuclear wastes. *J. Am. Ceram. Soc.* **105**, 6627–6639 (2022).

36. Cachia, J. N. *et al.* Enhancing cerium and plutonium solubility by reduction in borosilicate glass. *J. Nucl. Mater.* **352**, 182–189 (2006).

37. Feuchter, H. *et al.* Influence of light and temperature on the extractability of cerium(IV) as a surrogate of plutonium(IV) and its effect on the simulation of an accidental fire in the PUREX process. *ACS Omega* **4**, 12896–12904 (2019).
38. Lin, J., Cross, J. N., Diwu, J., Meredith, N. A. & Albrecht-Schmitt, T. E. Comparisons of plutonium, thorium, and cerium tellurite sulfates. *Inorg. Chem.* **52**, 4277–4281 (2013).
39. Zamoryanskaya, M. V & Burakov, B. E. Feasibility Limits in Using Cerium as a Surrogate for Plutonium Incorporation in Zircon, Zirconia and Pyrochlore. *MRS Online Proc. Libr.* **663**, 301 (2000).
40. Le Roux, S. & Jund, P. Ring statistics analysis of topological networks: New approach and application to amorphous GeS2 and SiO2 systems. *Comput. Mater. Sci.* **49**, 70–83 (2010).
41. Sivaraman, G. *et al.* A Combined Machine Learning and High-Energy X-ray Diffraction Approach to Understanding Liquid and Amorphous Metal Oxides. *J. Phys. Soc. Japan* **91**, 091009 (2022).
42. Minasian, S. G. *et al.* Quantitative Evidence for Lanthanide-Oxygen Orbital Mixing in CeO2, PrO2, and TbO2. *J. Am. Chem. Soc.* **139**, 18052–18064 (2017).
43. Guéneau, C. *et al.* Thermodynamic modelling of advanced oxide and carbide nuclear fuels: Description of the U-Pu-O-C systems. *J. Nucl. Mater.* **419**, 145–167 (2011).
44. Skinner, L. B. *et al.* A time resolved high energy X-ray diffraction study of cooling liquid SiO2. *Phys. Chem. Chem. Phys.* **15**, 8566–8572 (2013).
45. Soper, A. K. Inelasticity corrections for time-of-flight and fixed wavelength neutron diffraction experiments. *Mol. Phys.* **107**, 1667–1684 (2009).

460

Methods

Sample preparation and containment

Three PuO_{2-x} pellets were prepared by uniaxially pressing PuO_2 powder (>99% chemical purity) with stearic acid as a binder in a stainless steel die. Powder isotopically enriched with ^{242}Pu (>99.9% radionuclidic purity) was used to minimize radioactivity safety risks. The pressed pellets were heated at 280 K min^{-1} to bake out the binder and sintered at 1920 K for 1 h under vacuum in a Mo-lined graphite crucible, followed by air milling to round off the corners of the cylindrical pellets. The resulting samples were spheroid in shape with a diameter of ~2.5 mm, each 78-82 mg. Rietveld refinement of one pellet's X-ray diffraction pattern indicated a mixture of *f*-PuO_{2-x}, cubic α-Pu_2O_3, and hexagonal β-Pu_2O_3 with a mean composition of $PuO_{1.81}$, which is close to the composition $PuO_{1.82}$ previously identified for congruent evaporation[46]. Three samples were then loaded into a radioactive containment vessel inside a hermetically sealed chamber designed for aerodynamic levitation of nuclear fuel materials[13]. The sample containment vessel resided in an antechamber to the main chamber, which contained the levitation nozzle and several ports for laser, camera, pyrometer, and X-ray access and egress (see SI for further details on instrumentation and radiological safety procedures). The containment vessel also included two beads of NIST-standard CeO_2 mounted in epoxy, used for calibration of the sample-detector distance during X-ray measurements, and two ZrO_2 beads that were used for precise alignment of the levitation position, laser heating beam, and X-ray beam.

CeO_2 spheroids, ~2 mm in diameter and 70-80 mg, were prepared by melting CeO_2 powder (99.9%, Aldrich) in a copper hearth with a 10.6 μm laser.

X-ray total scattering

The aerodynamic levitator and chamber containing the samples were installed at Sector 6-ID-D of the Advanced Photon Source, Argonne National Laboratory (Argonne, IL, USA). A vacuum chuck integrated with the chamber was used to transfer samples between the containment vessel and the adjoining levitation chamber. The sample levitation position was aligned with the incoming X-ray beam, a video camera, and an optical pyrometer (λ = 0.9 μm, 975-3775 K, Chino) for temperature measurements. Sample emissivity was assumed to be 0.92 for pyrometer temperature correction, based on prior studies on molten oxides[47] (see SI). Diffraction of transmitted 99.959 keV X-rays passing through the top of the spheroid sample was measured with an area detector (Varex 4343CT), which was covered with a 1 mm thick brass sheet to preferentially attenuate Pu L-edge fluorescence near 23 keV. The X-ray beam at the sample position was 0.2 mm tall and 0.5 mm wide. Background diffraction measurements taken without a sample were used to subtract the scattering contributions from 1 mm thick silica windows on the chamber and the gas along the X-ray path. A small tungsten beam stop was placed immediately downstream of the silica exit window to further minimize its scattering, which blocked X-rays at scattering vectors below Q_{min} = 1.3 Å^{-1}. The detector was positioned at a distance from the sample of either 1320 or 420 mm. The longer distance provides better Q resolution for Bragg peaks, while the shorter distance achieves a larger Q range (up to 23.3 Å^{-1}) necessary for high resolution PDF analysis. For a given sample, heating and measurements of the solid were collected first using the 1320 mm detector distance. Then the sample was cooled and the detector was repositioned to 420 mm, followed by heating and liquid measurements.

Samples were levitated using a gas stream of either O_2, 1% O_2 (Ar balance), ultrahigh purity Ar, or 5% CO (Ar balance), and heated with a 10.6 μm laser (Synrad i401, spot diameter ~1mm

at sample position)[48]. Heating was increased incrementally, alternating with diffraction measurements of the sample held isothermally at temperatures ranging 1350-3000 K (Extended Data Fig. 3a). Measurements were not taken for heated samples below 1350 K due to reduced temperature stability in the lower range of laser power. The uncertainty in sample temperatures is estimated as ± 150 K for solids and ± 50 K for liquids (see SI).

X-ray diffraction measurements of CeO_{2-x} samples were collected in a similar setup, without the nuclear materials chamber.

Data analysis

The area detector distance and tilt were calibrated with Fit2D[49] using diffraction patterns of NIST-standard CeO_2. Sample diffraction patterns were then azimuthally integrated in Fit2D and corrected for flat field, X-ray polarization, oblique incidence and detector attenuation effects[50]. Background subtraction, sample attenuation and multiple scattering corrections, and subtraction of self and Compton scattering were performed using GudrunX[51] to obtain the normalized total X-ray structure factors, *S(Q)*[15]. The structure factor is a summation of the atomic partial pair structure factors, $s_{ij}(Q)$, for atom types i and j. These partials are weighted by the normalized Faber-Ziman weighting factors[52], $W_{ij}(Q)$:

$$S(Q) = \sum_{i,j \geq i} W_{ij}(Q) s_{ij}(Q) \quad (1)$$

$$W_{ij}(Q) = \frac{(2 - \delta_{ij}) c_i c_j f_i(Q) f_j(Q)}{\langle f(Q) \rangle^2} \quad (2)$$

where c_i are the fractional atomic concentrations and $f_i(Q)$ are the X-ray free-atom atomic form factors[53]. Weighting factors for all molten samples are given in Extended Data Table 1, for $Q = 0$ Å^{-1}, and plotted as functions of Q in Extended Data Fig. 4.

For measurements of solid samples, Rietveld refinements for crystalline phases were performed in GSAS-II[54] (Extended Data Fig. 5). X-ray diffraction patterns were compared against fluorite PuO_2 (*f*-PuO_2), α-Pu_2O_3, β-Pu_2O_3, PuO, and all phases of metallic Pu (α, β, γ, δ, δ', and ε). Instrument parameters were refined using NIST-standard CeO_2 and not modified during sample pattern refinement. Sample parameters were refined iteratively. First, the background was fitted. Next, the scaling factor and lattice parameter were refined, followed by crystallite size. These steps were followed first for the predominant phase *f*-PuO_{2-x} and then repeated for the minority phases. For the PuO_{2-x} phase, texture (preferred orientation) was also refined to improve the goodness-of-fit. Texture refinement is justified due to two known limitations of the levitation method for crystal X-ray diffraction: (i) quenching of levitated melts often results in a sample containing only a few crystallites of very large size, and (ii) the gas flow provides inconsistent rotation of the sample, so the diffraction pattern obtained is not a proper orientational average. The data resolution was insufficient to draw quantitative insights on crystallite size or texture, but the goal of refining these parameters was to improve accuracy of the lattice parameter and phase fraction determinations. For the initial material and recovered samples, mean compositions were calculated based on the phase fractions determined from Rietveld refinements.

For liquid measurements, the low-*Q* range of *S(Q)* below 1.4-1.5 $Å^{-1}$ was extrapolated by fitting a Lorentzian distribution to the first principal peak (Extended Data Fig. 6), while constraining the fit to match the theoretical value for *S(0)*[44], assuming isothermal compressibility is zero for the liquids. The "top hat" convolution[45] in GudrunX was used to reduce long-wavelength background in *S(Q)* that otherwise manifests as oscillations in the nonphysical region

549 of the PDFs at $r < 1$ Å (Extended Data Fig. 7). Then, the PDFs were obtained by the Fourier
550 transform:

$$G(r) = 1 + \frac{1}{2\pi^2 \rho r} \int_0^{Q_{max}} Q(S(Q) - 1) \sin(Qr)\, dQ \quad (3)$$

$$T(r) = 4\pi\rho r G(r) \quad (4)$$

551 For PuO_{2-x}, based on the signal-to-noise present in *S(Q)*, a Q_{max} of 17.4 $Å^{-1}$ was selected. Sample
552 density, ρ, ranged 0.0559-0.0572 atoms $Å^{-1}$ (9.28-9.65 g cm^{-3}) depending on sample
553 composition. For $CeO_{1.75}$, ρ = 0.0575 atoms $Å^{-1}$ (5.84 g cm^{-3}) and Q_{max} = 11.9 $Å^{-1}$. These density
554 values were estimated from the low-*r* slope in *T(r)* and are within 5% of estimates based on
555 literature data for the high-temperature crystals and anticipated volume changes upon melting.
556 (See SI for further discussion.)

557 Sample compositions in the *f*-PuO_{2-x} phase were calculated using the relationship with gas
558 pO_2[14] (see SI for discussion of composition calculations and uncertainty). For *f*-CeO_{2-x}, the
559 composition-pO_2 relationship was extrapolated from experimental data[32]. Because oxygen
560 activity is not known for the liquids, the liquid compositions were assigned the values present at
561 the liquidi.

562 NXFit[55] was used to fit Gaussian distributions, convolved with the correct peak-shape
563 functions, to the total PDFs, from which mean bond distances and coordination numbers were
564 extracted (Extended Data Fig. 1).

565

566 **Empirical potential structure refinement**

567 Structural models for molten $PuO_{1.76}$ and $CeO_{1.75}$ were obtained using EPSR[22,56]. The EPSR
568 technique begins by defining a simulation volume of specified composition, density, and
569 temperature. Atomic positions are initially equilibrated using Lennard-Jones and pseudo-

570 Coulomb potentials, after which the X-ray scattering data are introduced in a reverse Monte
571 Carlo simulation that refines the interatomic potentials to bring the model toward agreement with
572 experimental scattering data (the so-called "empirical potential"). Each model was initialized
573 with a mixture of 3+ and 4+ oxidation states for the cations, with the atomic concentrations set to
574 match the compositions. A simulation box containing 1596 atoms (ρ = 0.0571 atoms Å^{-3} for
575 $PuO_{1.76}$ or 0.0575 atoms Å^{-3} for $CeO_{1.75}$, edge length ~30.3 Å) was equilibrated using the
576 pairwise potentials given in Supplementary Table 1 in the SI. For O^{2-}, the potential parameters
577 were taken from prior EPSR models for metal oxide liquids[57,58] and adjusted slightly to improve
578 agreement between the equilibrated model (without empirical potential) and the X-ray scattering
579 data. For Pu(III) and Pu(IV), the Lennard-Jones atomic radii (σ) were chosen so that the cation-
580 oxygen pairs had bond distances that matched those obtained from Gaussian peak fitting of the
581 PDFs (Extended Data Fig. 1), again with slight adjustments to improve the equilibrated model.
582 Values were explored for the cations' ε parameters ranging 1.0-2.3, but the final model (after
583 empirical potential) was not significantly influenced. The chosen values (1.5 kJ mol^{-1}) are within
584 the range of cations used in other oxide liquid models[58]. For consistency, the same reference
585 potentials were applied for Ce(III) and Ce(IV) as for Pu(III) and Pu(IV).
586 After at least 10,000 step iterations to equilibrate the models at 3000 K, the X-ray structure
587 factors were introduced to drive refinement of the so-called "empirical potential" with EPSR's
588 reverse Monte Carlo approach, which improves the model's agreement with the X-ray data.
589 The scattering data were introduced as an empirical potential and applied at a magnitude of 10-
590 20% of the system energy. After at least 10,000 iterations, the structure factor of the model was
591 calculated and averaged over an additional 7,500 iterations.

To analyze the short- and intermediate-range atomic order, a cutoff distance of 3.21 Å was used for Pu-O and Ce-O, corresponding to the minima in the atomic partial pair correlation after its first peak. Connectivity between Pu-O or Ce-O polyhedra was assessed by counting the number of O shared between neighboring cations. Bond angle distributions, coordination number distributions, and ring statistics[40] according to King's criterion[59] were calculated using Atomes[60]. Bond angle distributions are normalized by the *sin(θ)* dependence that would occur for a random distribution.

Sensitivity of the model to initial reference potentials, temperature, and composition is discussed in the SI.

Density functional theory

Spin polarized DFT calculations were performed with the plane-wave Vienna *ab initio* simulation package (VASP) using projected augmented wave (PAW) pseudo-potentials[61,62]. The exchange correlation term was modelled using the generalized gradient approximation (GGA) of Perdew, Burke and Ernzeroff (PBE)[63]. A plane wave cutoff of 650 eV was found to be suitable[64], and an electronic convergence criterion of 10^{-6} eV was used. A Γ-centered 1×1×1 k mesh was used for reciprocal sampling. To accurately describe the behavior of the localized Pu 5*f* states, the orbital-dependent Coulomb potential (U) and exchange parameter (J) were applied within the rotationally invariant DFT+U formalism of Liechtenstein *et al.*[65], with U = 4.5 eV and J = 0.5 eV[66,67]. A Grimme "D3" dispersion correction was included[68,69].

Gaussian approximation potential and molecular dynamics

A machine-learned Gaussian approximation potential[30] (GAP) was developed using two-body squared-exponential and many-body smooth overlap of atomic positions (SOAP) kernel functions[70,71] to measure chemical similarity between local chemical neighborhoods. To create a diverse training database, we utilized a previously developed active learning framework that can generate ultrafast sampling on small unit cells (i.e., 10s to 100s of atoms) using empirical force fields, followed by single point DFT+U[31,72,73]. The procedure was further iterated on generations of GAP models, leading to sufficient coverage of the training database[74,75].

To begin training, 75-atom unit cells of PuO_2 were melted with the available empirical force fields[12,76,77], starting with either (i) randomly packed atoms generated using packmol, or (ii) crystalline *f*-PuO_2. The structures were thermalized at 5000 K to ensure full melting, equilibrated to 3600 K, and then active learning was applied to ~15 ps trajectories sampled at 3600 K. To improve the diversity of the training database, samples were also drawn from *f*-PuO_2 at 300, 500, 1500, and 3000 K. DFT+U single point calculations were performed, and an initial GAP model was generated. With this model, liquid structures for the experimentally measured compositions ($PuO_{1.76}$, $PuO_{1.69}$, and $PuO_{1.57}$) were then sampled, starting from packmol generated inputs, followed by single point DFT+U and iterative retraining. Details of the final training database and GAP hyperparameters are summarized in Supplementary Tables 2 and 3 of the SI, respectively. The GAP model validated on 52 independent test samples showed a root mean square error in energy and force of 7.68 meV atom^{-1} and 0.45 eV Å^{-1}, respectively.

The GAP model was used to perform MD simulations of $PuO_{1.76}$ with a system size of 2,160 atoms at the same density as the experimental measurement, 0.0571 atoms Å^{-3} (simulation box edge length of 33.57 Å). MD was performed using the LAMMPS software package compiled with the QUIP pair style[78,79]. The system was initially thermalized at 3600 K in the NVT

ensemble[80,81] and equilibrated at 3000 K. The NVT simulation was continued at 3000 K for 1.1 ns with a timestep of 0.5 fs, and the last 1 ns was used for structure calculations.

For PDOS calculations from the GAP-MD model, a smaller simulation box containing 80 atoms was used to aid convergence of the DFT+U calculations. More than 30 liquid structures at 3000 K were sampled with this approach, and the PDOS was averaged across this set of configurations.

Data availability

X-ray structure factor data for the $PuO_{1.76}$ and $CeO_{1.75}$ melts are provided in the Supplementary Information. All other relevant data are available from the corresponding author upon reasonable request.

46. Messier, D. R. Evaporation of Hypostoichiometric Plutonium Dioxide from 2070° to 2380°K. *J. Am. Ceram. Soc.* **51**, 710–713 (1968).

47. Krishnan, S., Weber, J. K. R., Schiffman, R. A., Nordine, P. C. & Reed, R. A. Refractive Index of Liquid Aluminum Oxide at 0.6328 μm. *J. Am. Ceram. Soc.* **74**, 881–883 (1991).

48. Weber, J. K. R., Benmore, C. J., Jennings, G., Wilding, M. C. & Parise, J. B. Instrumentation for fast in-situ X-ray structure measurements on non-equilibrium liquids. *Nucl. Instruments Methods Phys. Res. A* **624**, 728–730 (2010).

49. Hammersley, A. P. FIT2D: a multi-purpose data reduction, analysis and visualization program. *J. Appl. Crystallogr.* **49**, 646–652 (2016).

50. Skinner, L. B., Benmore, C. J. & Parise, J. B. Area detector corrections for high quality synchrotron X-ray structure factor measurements. *Nucl. Instruments Methods Phys. Res. A*

662, 61–70 (2012).

51. Soper, A. K. & Barney, E. R. Extracting the pair distribution function from white-beam X-ray total scattering data. *J. Appl. Crystallogr.* **44**, 714–726 (2011).

52. Faber, T. E. & Ziman, J. M. A theory of the electrical properties of liquid metals. *Philos. Mag. A J. Theor. Exp. Appl. Phys.* **11**, 153–173 (1965).

53. Waasmaier, D. & Kirfel, A. New analytical scattering-factor functions for free atoms and ions. *Acta Crystallogr.* **A51**, 416–431 (1995).

54. Toby, B. H. & Von Dreele, R. B. GSAS-II: the genesis of a modern open-source all purpose crystallography software package. *J. Appl. Crystallogr.* **46**, 544–549 (2013).

55. Pickup, D., Moss, R. & Newport, R. NXFit: A program for simultaneously fitting X-ray and neutron diffraction pair-distribution functions to provide optimized structural parameters. *J. Appl. Crystallogr.* **47**, 1790–1796 (2014).

56. Wilke, S. K., Alderman, O. L. G., Benmore, C. J., Neuefeind, J. & Weber, R. Octahedral oxide glass network in ambient pressure neodymium titanate. *Sci. Rep.* **12**, 8258 (2022).

57. Alderman, O. L. G., Skinner, L. B., Benmore, C. J., Tamalonis, A. & Weber, J. K. R. Structure of molten titanium dioxide. *Phys. Rev. B* **90**, 094204 (2014).

58. Alderman, O. L. G., Benmore, C. J., Neuefeind, J., Tamalonis, A. & Weber, R. Molten barium titanate: A high-pressure liquid silicate analogue. *J. Phys. Condens. Matter* **31**, 20LT01 (2019).

59. King, S. V. Ring Configurations in a Random Network Model of Vitreous Silica. *Nature* **213**, 1112–1113 (1967).

60. Roux, S. Le. Atomes. https://atomes.ipcms.fr/ (2023).

61. Kresse, G. & Furthmüller, J. Efficient iterative schemes for ab initio total-energy

calculations using a plane-wave basis set. *Phys. Rev. B* **54**, 11169–11186 (1996).

62. Kresse, G. & Joubert, D. From ultrasoft pseudopotentials to the projector augmented-wave method. *Phys. Rev. B* **59**, 1758–1775 (1999).

63. Perdew, J. P., Burke, K. & Ernzerhof, M. Generalized Gradient Approximation Made Simple. *Phys. Rev. Lett.* **77**, 3865–3868 (1996).

64. Chen, J.-L. & Kaltsoyannis, N. DFT + U Study of Uranium Dioxide and Plutonium Dioxide with Occupation Matrix Control. *J. Phys. Chem. C* **126**, 11426–11435 (2022).

65. Liechtenstein, A. I., Anisimov, V. I. & Zaanen, J. Density-functional theory and strong interactions: Orbital ordering in Mott-Hubbard insulators. *Phys. Rev. B* **52**, R5467–R5470 (1995).

66. Wang, H. & Konashi, K. LDA+U study of Pu and PuO2 on ground state with spin–orbital coupling. *J. Alloys Compd.* **533**, 53–57 (2012).

67. Cooper, M. W. D. *et al.* Development of Xe and Kr empirical potentials for CeO2, ThO2, UO2 and PuO2, combining DFT with high temperature MD. *J. Phys. Condens. Matter* **28**, 405401 (2016).

68. Grimme, S., Antony, J., Ehrlich, S. & Krieg, H. A consistent and accurate ab initio parametrization of density functional dispersion correction (DFT-D) for the 94 elements H-Pu. *J. Chem. Phys.* **132**, 154104 (2010).

69. Grimme, S., Ehrlich, S. & Goerigk, L. Effect of the damping function in dispersion corrected density functional theory. *J. Comput. Chem.* **32**, 1456–1465 (2011).

70. Bartók, A. P., Kondor, R. & Csányi, G. On representing chemical environments. *Phys. Rev. B* **87**, 184115 (2013).

71. Deringer, V. L. & Csányi, G. Machine learning based interatomic potential for amorphous

carbon. *Phys. Rev. B* **95**, 94203 (2017).

72. Sivaraman, G. *et al.* Machine-learned interatomic potentials by active learning: amorphous and liquid hafnium dioxide. *npj Comput. Mater.* **6**, 104 (2020).

73. Sivaraman, G. *et al.* Automated Development of Molten Salt Machine Learning Potentials: Application to LiCl. *J. Phys. Chem. Lett.* **12**, 4278–4285 (2021).

74. Guo, J. *et al.* Composition-transferable machine learning potential for LiCl-KCl molten salts validated by high-energy x-ray diffraction. *Phys. Rev. B* **106**, 14209 (2022).

75. Guo, J. *et al.* AL4GAP: Active learning workflow for generating DFT-SCAN accurate machine-learning potentials for combinatorial molten salt mixtures. *J. Chem. Phys.* **159**, 24802 (2023).

76. Cooper, M. W. D., Rushton, M. J. D. & Grimes, R. W. A many-body potential approach to modelling the thermomechanical properties of actinide oxides. *J. Phys. Condens. Matter* **26**, 105401 (2014).

77. Cooper, M. W. D., Murphy, S. T., Fossati, P. C. M., Rushton, M. J. D. & Grimes, R. W. Thermophysical and anion diffusion properties of (Ux,Th1-x)O2. *Proc. R. Soc. A Math. Phys. Eng. Sci.* **470**, 20140427 (2014).

78. Plimpton, S. Fast Parallel Algorithms for Short-Range Molecular Dynamics. *J. Comput. Phys.* **117**, 1–19 (1995).

79. Csányi, G. *et al.* Expressive programming for computational physics in Fortran 95+. *IoP Comput. Phys. Newsl.* (2007).

80. Nosé, S. A unified formulation of the constant temperature molecular dynamics methods. *J. Chem. Phys.* **81**, 511–519 (1984).

81. Hoover, W. G. Canonical dynamics: Equilibrium phase-space distributions. *Phys. Rev. A*

729 **31**, 1695–1697 (1985).

730

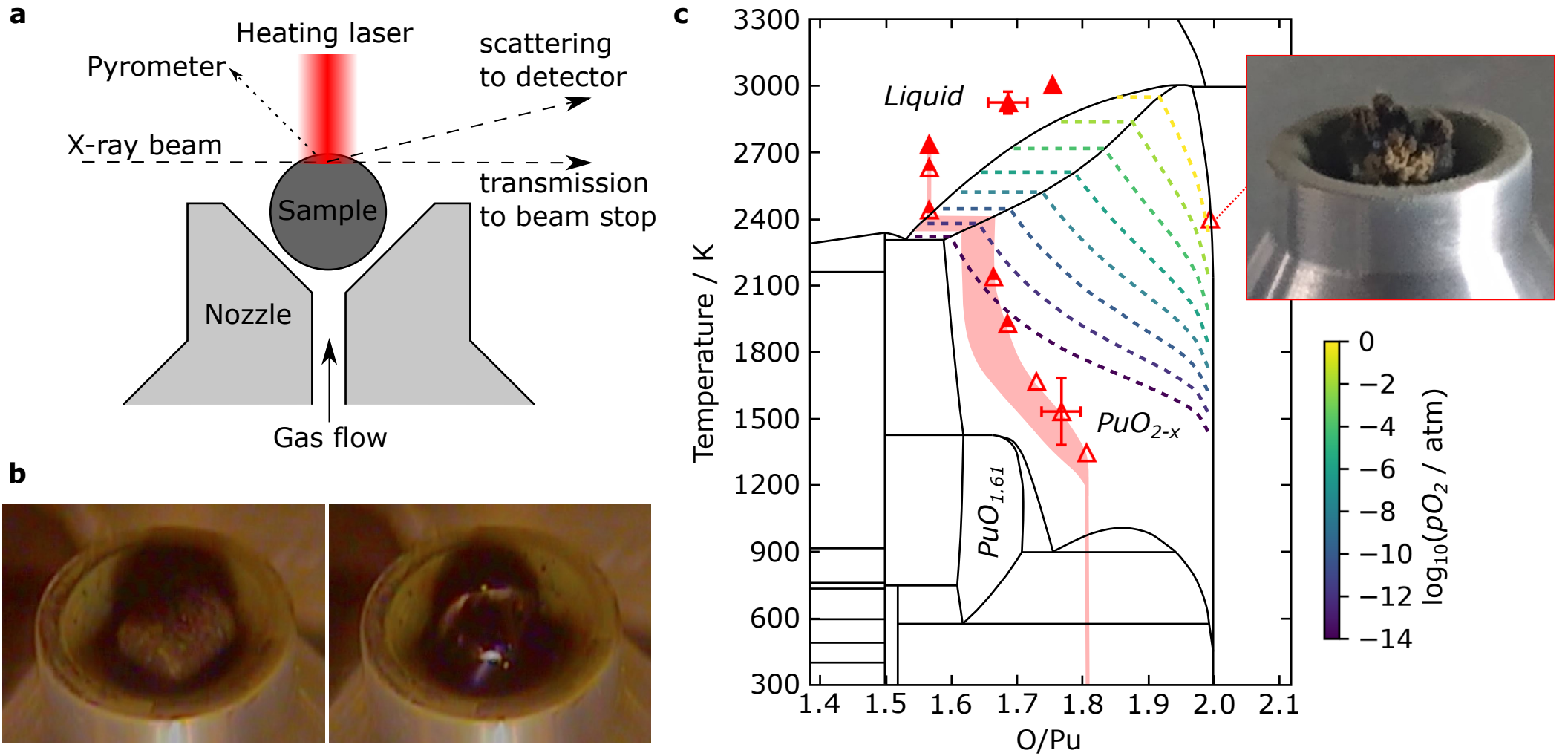
a
Heating laser
Pyrometer
scattering
to detector
X-ray beam
transmission
to beam stop
Sample
Nozzle
Gas flow
b
c
Liquid
PuO_{2-x}
$PuO_{1.61}$
Temperature / K
O/Pu
3300
3000
2700
2400
2100
1800
1500
1200
900
600
300
1.4
1.5
1.6
1.7
1.8
1.9
2.0
2.1
0
−2
−4
−6
−8
−10
−12
−14
$\log_{10}(pO_2$ / atm)

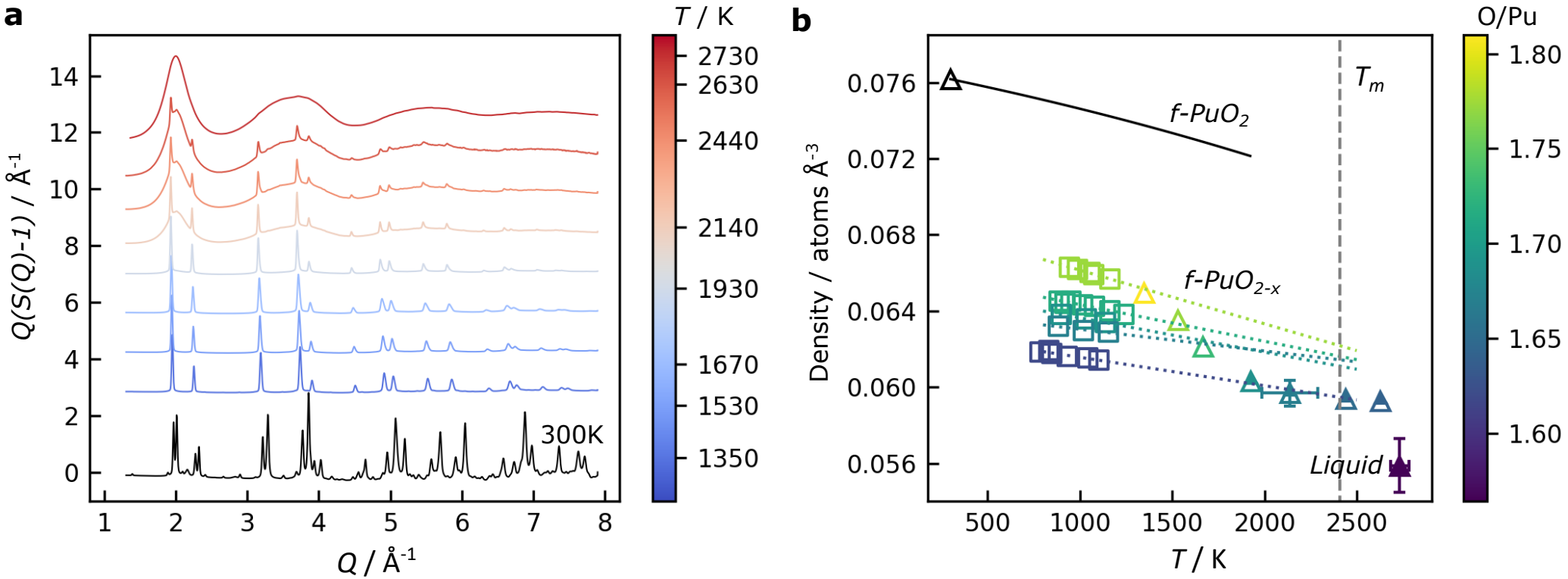
a
Q(S(Q)-1) / Å-1
Q / Å-1
T / K
2730
2630
2440
2140
1930
1670
1530
1350
300K
b
Density / atoms Å-3
T / K
f-PuO2
f-PuO2-x
Tm
Liquid
O/Pu
1.80
1.75
1.70
1.65
1.60

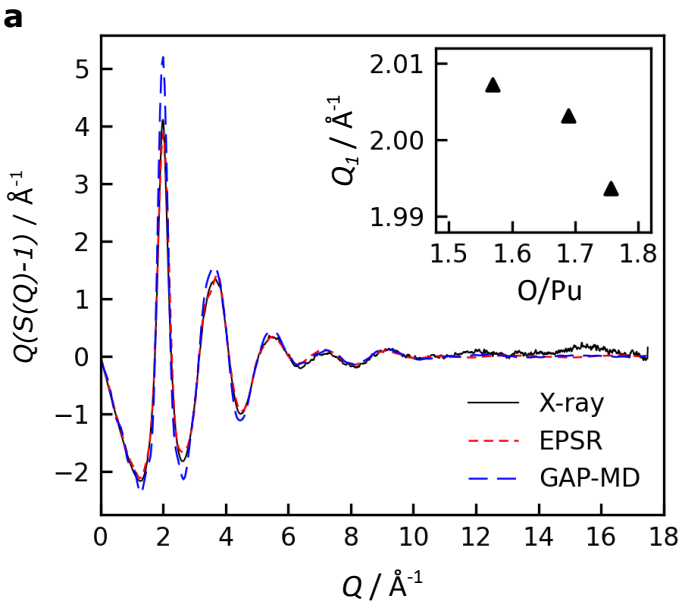

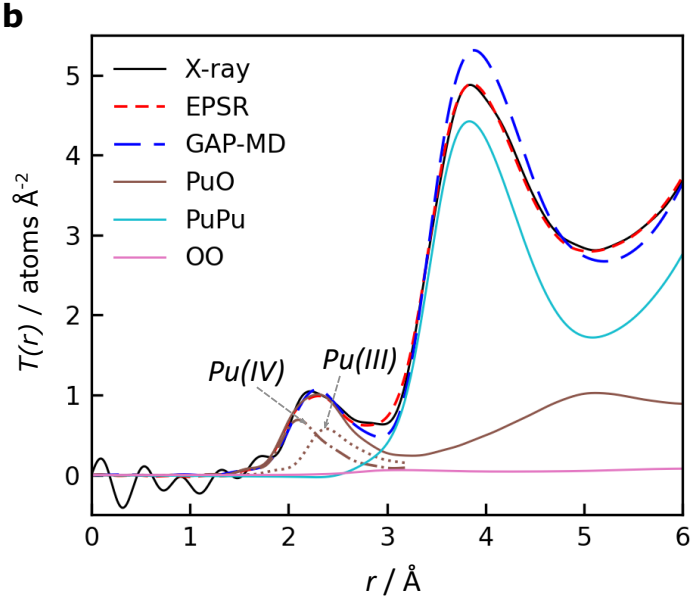

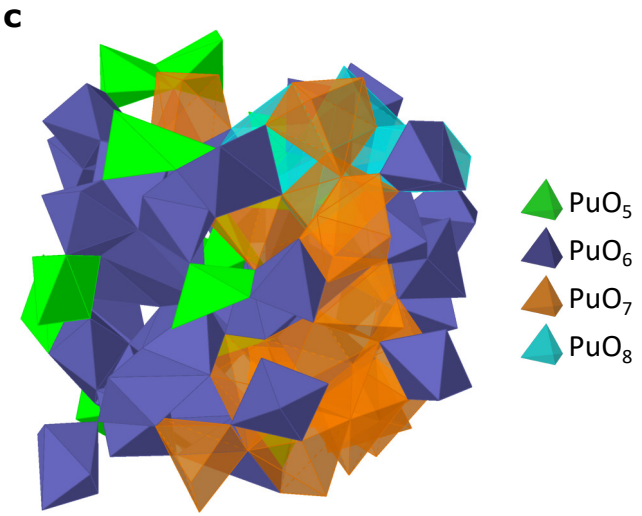

d

	r_{PuO} (Å)	n_{PuO}	r_{PuPu} (Å)	n_{PuPu}
Peak fit	2.399	6.5(3)	3.829	8.6(4)
EPSR	2.421	5.9(4)	4.105	8.5(5)
f-PuO_2	2.337	8	3.817	12
α-Pu_2O_3	2.295-2.401	6	3.667-4.059	12

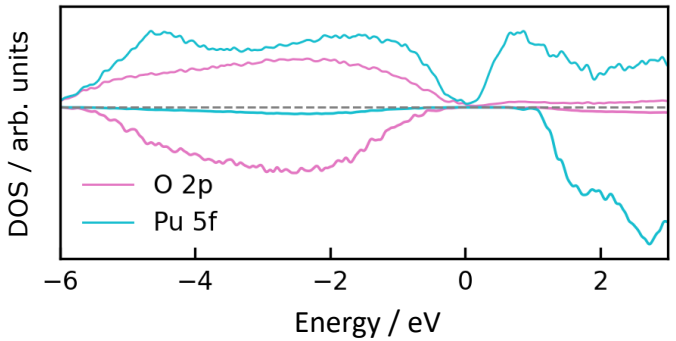

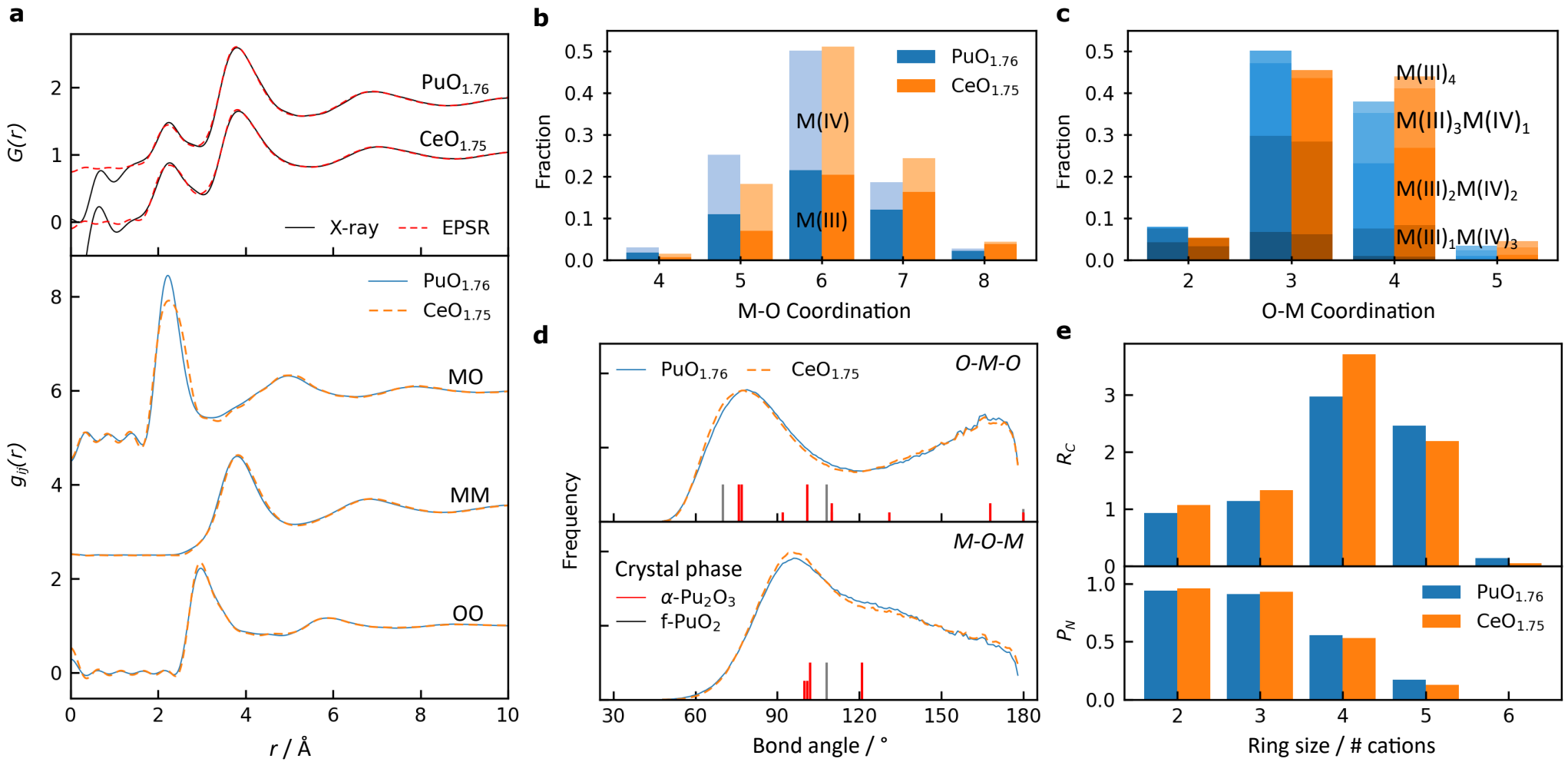
a
G(r)
PuO1.76
CeO1.75
X-ray
EPSR
gij(r)
PuO1.76
CeO1.75
MO
MM
OO
r / Å
b
Fraction
PuO1.76
CeO1.75
M(IV)
M(III)
M-O Coordination
c
Fraction
M(III)4
M(III)3M(IV)1
M(III)2M(IV)2
M(III)1M(IV)3
O-M Coordination
d
Frequency
PuO1.76
CeO1.75
O-M-O
M-O-M
Crystal phase
α-Pu2O3
f-PuO2
Bond angle / °
e
RC
PN
PuO1.76
CeO1.75
Ring size / # cations

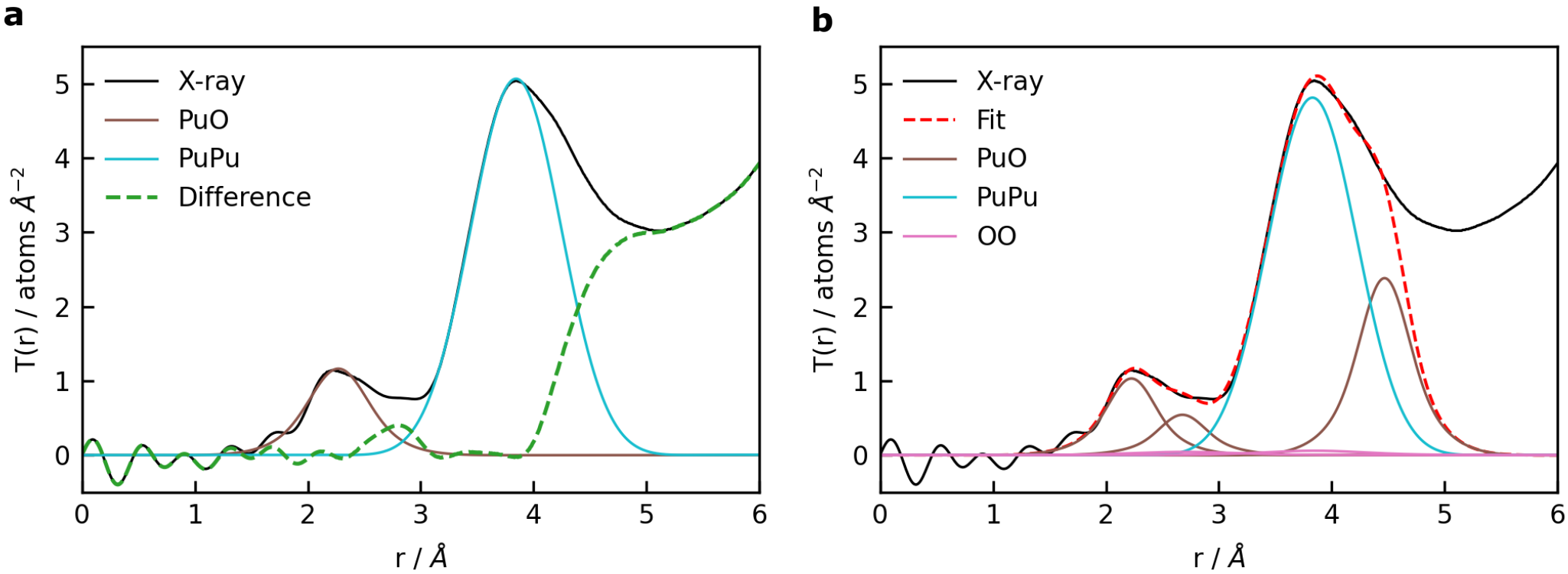
a
X-ray
PuO
PuPu
Difference
T(r) / atoms Å^{-2}
r / Å
b
X-ray
Fit
PuO
PuPu
OO
T(r) / atoms Å^{-2}
r / Å

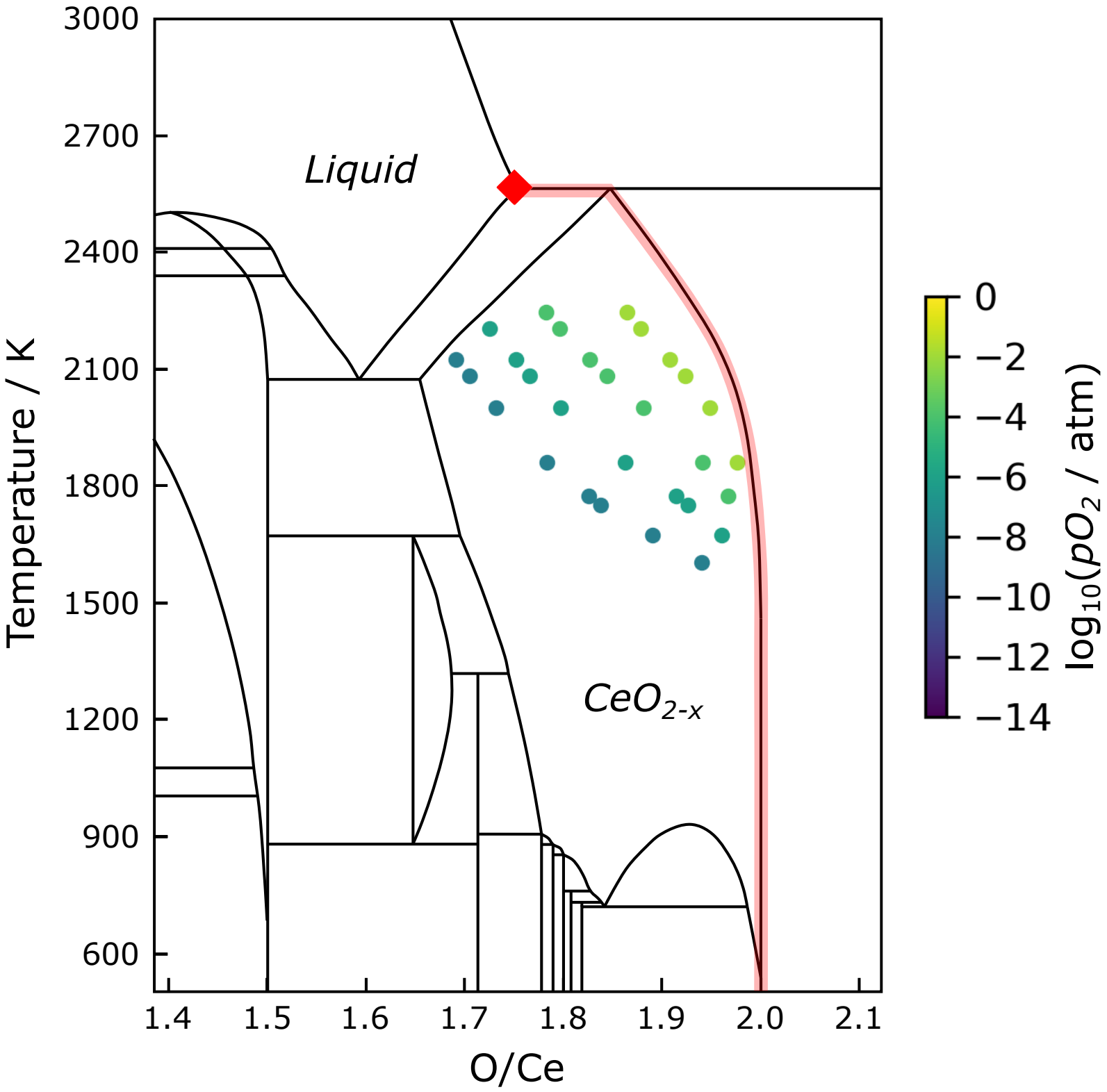
3000
2700
2400
2100
1800
1500
1200
900
600
Temperature / K
Liquid
CeO_{2-x}
1.4
1.5
1.6
1.7
1.8
1.9
2.0
2.1
O/Ce
0
−2
−4
−6
−8
−10
−12
−14
$\log_{10}(pO_2$ / atm)

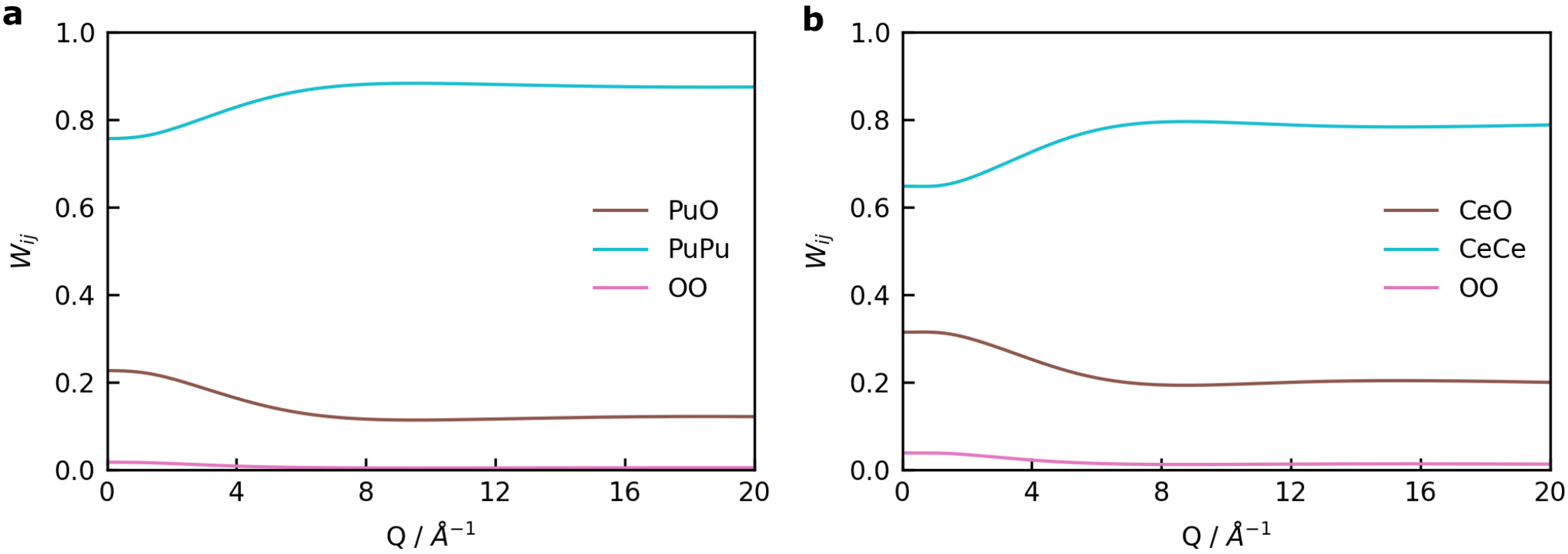
a
1.0
0.8
0.6
0.4
0.2
0.0
W_{ij}
PuO
PuPu
OO
0
4
8
12
16
20
Q / $Å^{-1}$
b
1.0
0.8
0.6
0.4
0.2
0.0
W_{ij}
CeO
CeCe
OO
0
4
8
12
16
20
Q / $Å^{-1}$

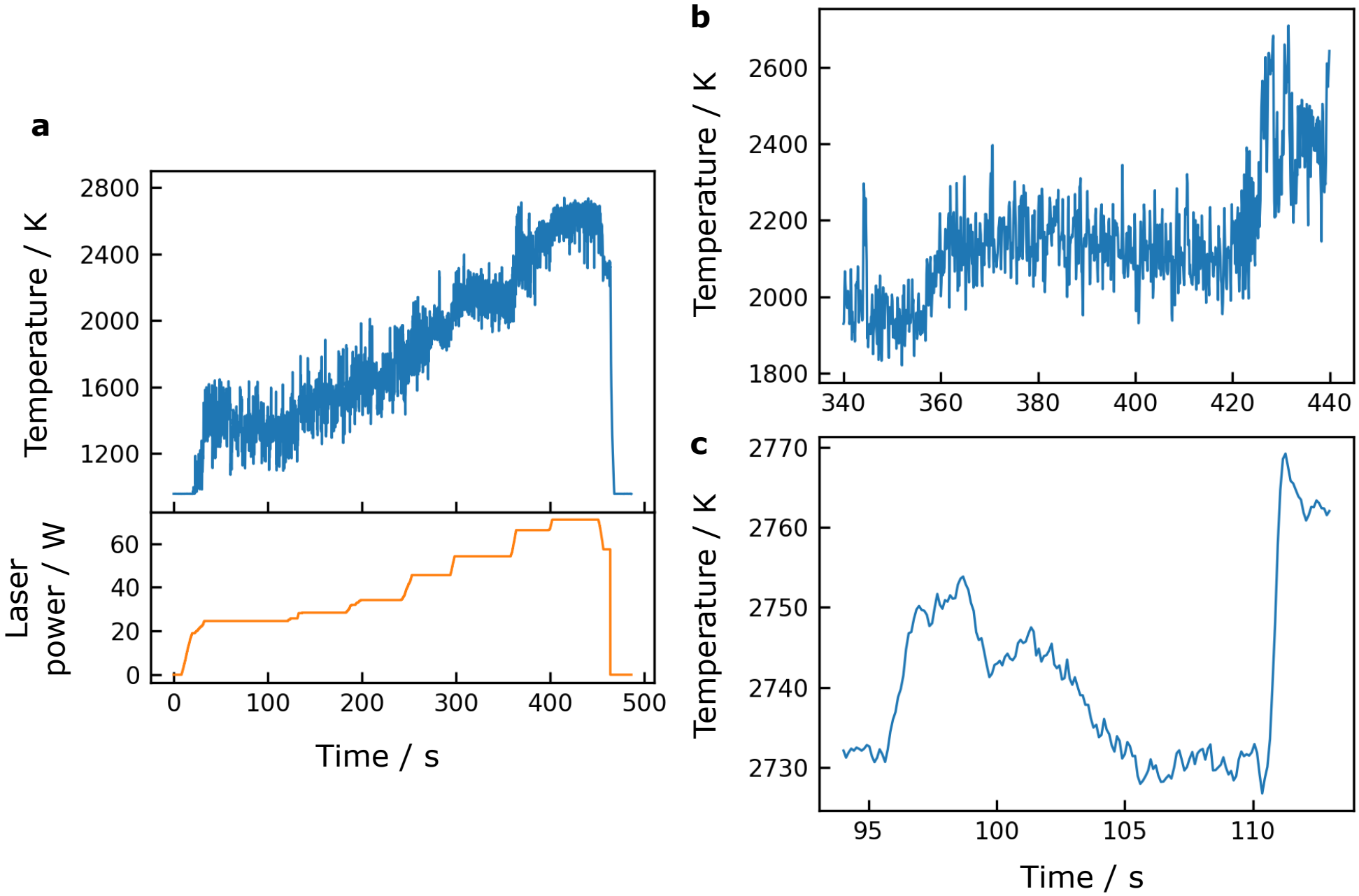
a
Temperature / K
2800
2400
2000
1600
1200
Laser power / W
60
40
20
0
0
100
200
300
400
500
Time / s
b
Temperature / K
2600
2400
2200
2000
1800
340
360
380
400
420
440
c
Temperature / K
2770
2760
2750
2740
2730
95
100
105
110
Time / s

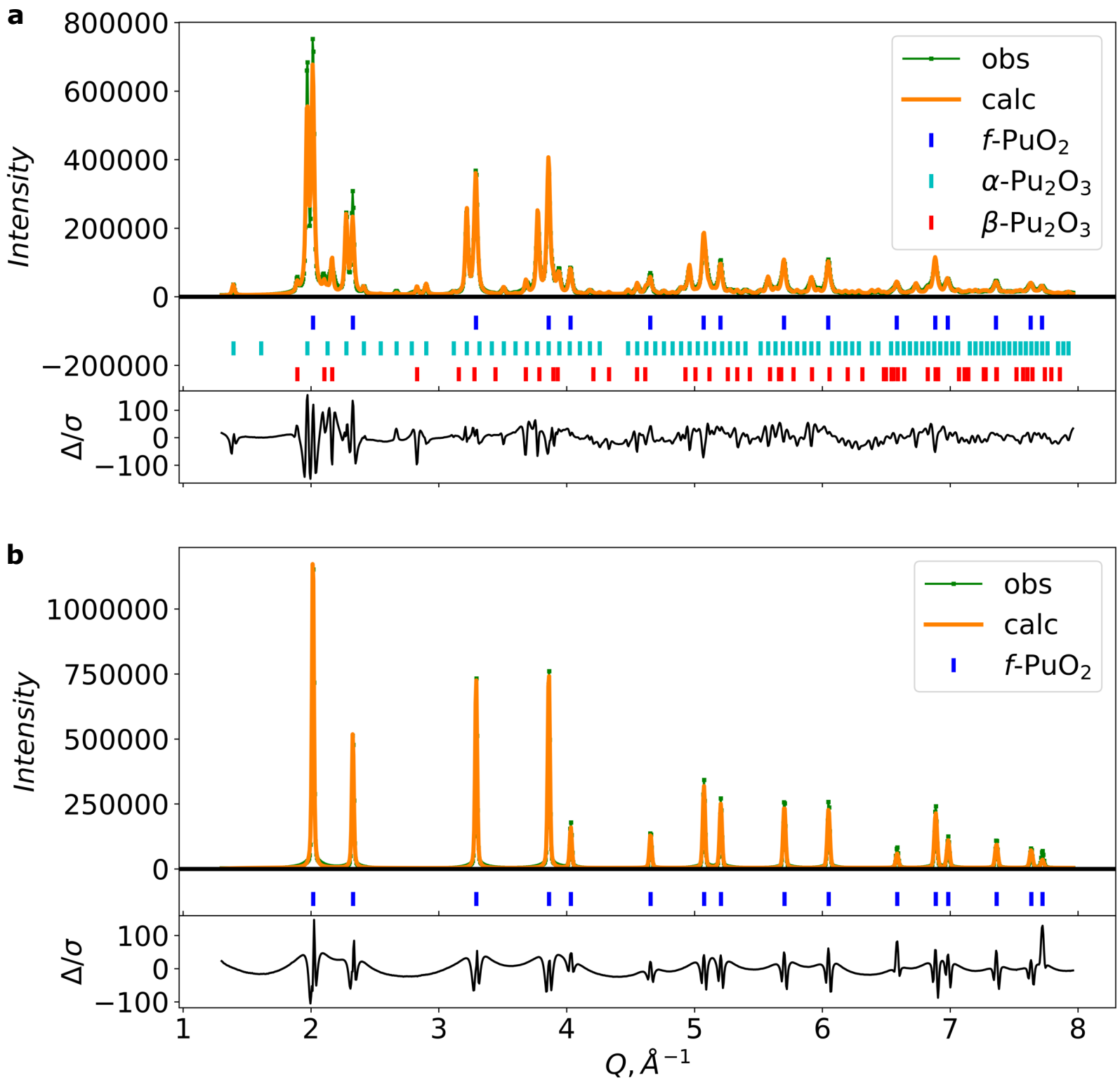
a
800000
600000
400000
200000
0
−200000
Intensity
obs
calc
f-PuO2
α-Pu2O3
β-Pu2O3
100
0
−100
Δ/σ
b
1000000
750000
500000
250000
0
Intensity
obs
calc
f-PuO2
100
0
−100
Δ/σ
1
2
3
4
5
6
7
8
Q, Å−1

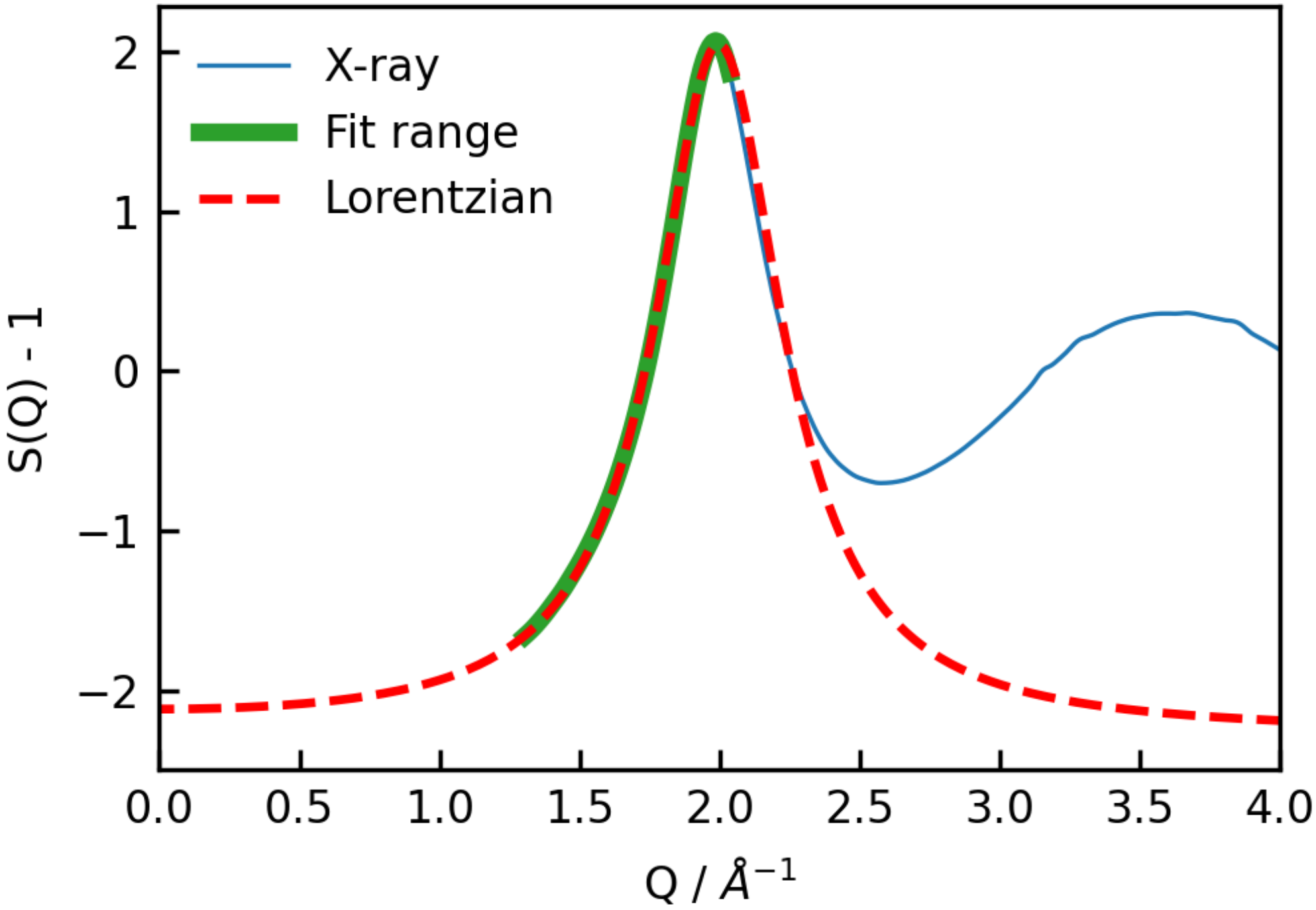
X-ray
Fit range
Lorentzian
S(Q) - 1
2
1
0
−1
−2
0.0
0.5
1.0
1.5
2.0
2.5
3.0
3.5
4.0
Q / Å^{-1}

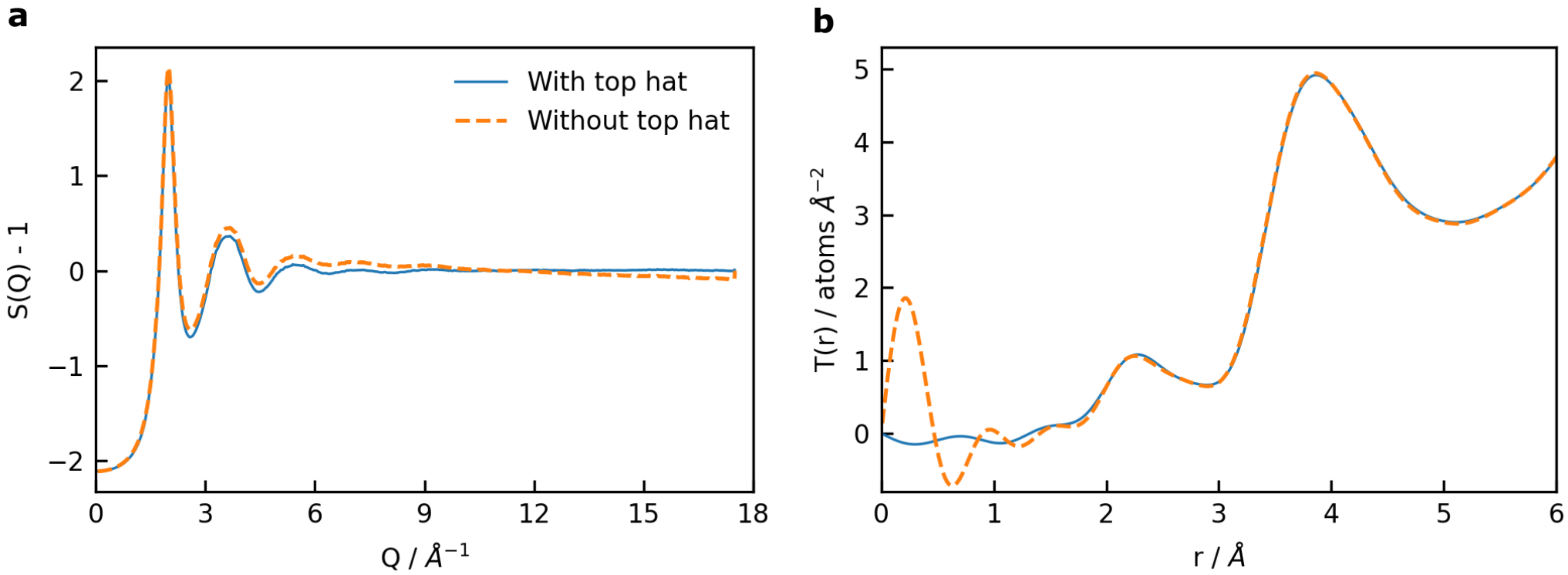
a
b
With top hat
Without top hat
S(Q) - 1
Q / Å^{-1}
T(r) / atoms Å^{-2}
r / Å
2
1
0
−1
−2
0
3
6
9
12
15
18
5
4
3
2
1
0
0
1
2
3
4
5
6

	$\mathbf{PuO_{1.57}}$	$\mathbf{PuO_{1.69}}$	$\mathbf{PuO_{1.76}}$	$\mathbf{CeO_{1.75}}$
W_{MO}	20.78	21.98	22.63	31.33
W_{MM}	77.83	76.44	75.68	64.89
W_{OO}	1.39	1.58	1.69	3.78

Table of Contents

I. Tables referenced by main text

Supplementary Table 1. Parameters for initial atomic reference potentials in EPSR.

Ion	Charge (e)	ε (kJ mol^{-1})	σ (Å)
Pu(III), Ce(III)	+1.5	1.5	2.22
Pu(IV), Ce(IV)	+2	1.5	1.62
O^{2-}	-1	0.92	3.38

Supplementary Table 2. GAP training database.

System	Number of Samples
Melt	444
Crystal	70
Isolated atoms	2
Total	516

Supplementary Table 3. GAP model hyperparameters.

Parameter	Two-body	SOAP
Cutoff (Å)	5.187	5.187
Sparse method	Uniform	CUR
Sparse points	50	1400
Delta (eV)	26.71	0.62
(l_{max}, n_{max})	--	(4, 11)

II. Levitation instrument

The X-ray scattering experiments used an aerodynamic levitation instrument specifically designed for the safe handling of nuclear fuel materials at very high temperatures and into the molten state. The instrument was essentially the same as described previously[1,2], so only an overview of its design and function is provided here. The only significant difference from the previously published instrument descriptions is the use of a double laser window assembly, described below.

The instrument design is shown in Supplementary Fig. 1 and comprises two main pieces: (1) the aerodynamic levitation chamber, and (2) the sample containment antechamber. (Component numbers given in the text match those annotated in Supplementary Fig. 1.) In the levitation chamber, gas is fed through a (3) converging-diverging nozzle, upon which the sample levitates. The levitation chamber contains several ports for (4) pyrometer, (5) video camera, (6) X-ray beam entry, (7) X-ray exit, and (8) two visual observation ports. These ports are all sealed with standard NW fittings, rubber O-rings, and silica windows. The pyrometer and video camera ports are positioned at 45° angles relative to the vertical, and the central axis of each of these ports aligns with the sample levitation position. Brass tubes with a ~6 mm inner diameter fill the X-ray entry port from the outer silica window to the wall of the levitation chamber, which aids in X-ray beam collimation. The X-ray exit window is thin (1 mm silica), and a tungsten beam stop is placed immediately outside the exit window, which minimizes window scattering contributions to the detector. At the top of the levitation chamber is (9) a cross purge assembly. One side port of the cross purge is attached to a one-way check valve, through which purge gas enters the chamber (2 SLM flow rate, same composition gas as used for levitation). The port on the opposite side of the cross purge is connected to a HEPA filter, through which the gas exits to a pump. The pump inlet is equipped with a variable conductance valve and pressure gauge, which are used to maintain the chamber pressure near 0.92 bar absolute pressure via closed loop control.

The (2) sample containment antechamber has a side port that is connected to (10) a stainless steel bellows with an integrated vacuum chuck. The vacuum chuck includes a 0.5 μm filter to prevent pieces of the sample from possibly being pulled into the diaphragm pump. The flexible bellows allows the user to manipulate the vacuum chuck to move samples between (11) the sample holder and the levitation position. When the bellows are compressed or extended, the closed loop controller on the vacuum pump valve restores the chamber pressure to near 0.92 bar. The sample holder (Supplementary Fig. 1c) resides in the antechamber and contains an array of wells, each containing a sample and covered by a perforated rubber gasket (not shown in Supplementary Fig. 1c). Three of the wells are used for the PuO_{2-x} samples, and these are covered with an additional (12) metal plate during transportation of the instrument to and from the X-ray synchrotron facility. The other wells contain ZrO_2 used for laser alignment and CeO_2 used for X-ray calibration of the sample-to-detector distance.

The top of the cross purge (on the levitation chamber) is connected to (13) a tube containing a stack of baffles, which decrease the transport of any volatilized sample onto the laser window. Above the baffles, a (14) tee assembly is connected that contains (15) two ZnSe windows for laser entry and (16) a side port. The side port is connected to an electronic pressure gauge and a needle

valve, through which the tee is pressurized to 1.1 bar absolute pressure. The heating laser enters through the top laser window and travels vertically downward to the sample position.

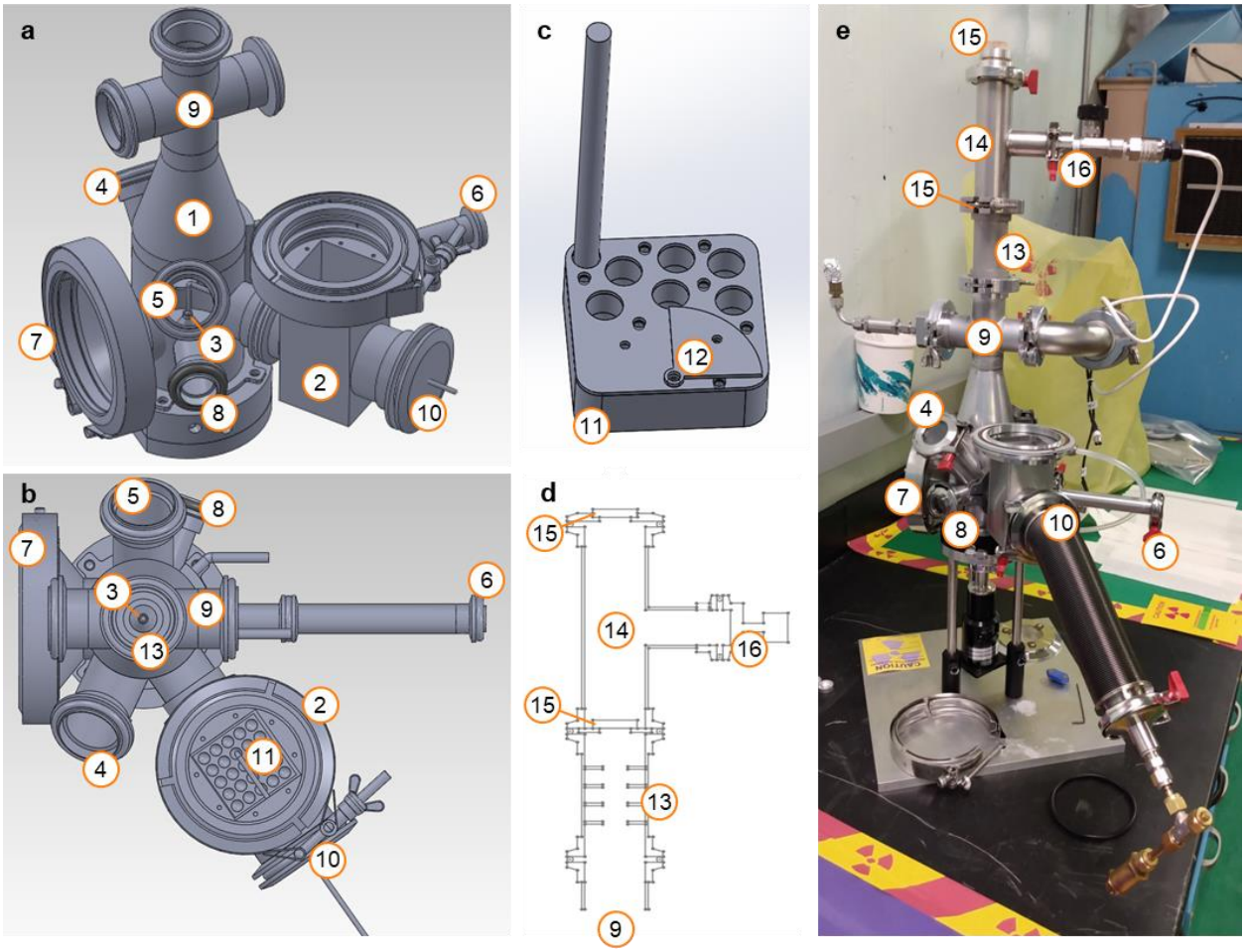

Supplementary Fig. 1. Levitation instrument used for X-ray scattering experiments. a, Isometric and **b,** top views (not showing the upper baffles and tee in (**d**)); **c,** sample holder; **d,** baffles and double window tee assembly; **e,** picture of the mostly assembled instrument. Components are numbered as described in the SI text: (1) levitation chamber, (2) sample containment antechamber, (3) levitation nozzle, (4) video camera port, (5) pyrometer port, (6) X-ray entry port, (7) X-ray exit port, (8) two ports for visual observation, (9) cross purge assembly, (10) port for sample manipulator, (11) sample holder, (12) metal cover lid for PuO_{2-x} samples, (13) baffles, (14) double laser window tee assembly, (15) two laser windows, (16) pressure gauge and needle valve. Drawings in (a) and (b) are adapted with permission from Benmore *et al.*[3]

III. Sample handling and radiological safety

A major challenge in this work was designing and implementing safety procedures for working with PuO_{2-x} in the X-ray synchrotron facility, which is not generally used as a radiologically controlled area. Safety board approval was required since the three ~80 mg PuO_{2-x} samples exceeded the policy limits for the X-ray facility. This approval was obtained only after thorough safety reviews of the instrument design, failure analysis, operational validation testing, engineering controls, and administrative controls. Only the major aspects are summarized here.

Samples were made containing ^{242}Pu (>99.9% radionuclidic purity), which was selected to minimize the radioactivity (compared to other Pu isotopes).

The instrument design included features to guard against several potential failure modes. One major concern was the deposition of volatilized sample onto the laser window, since any deposited sample would absorb the laser, heat up, and potentially rupture the window and cause a breach of the containment vessel. The gas cross purge and stacked baffles were designed to eliminate any volatilized sample from reaching the laser window. Additionally, a double laser window assembly was implemented to prevent a breach even in the scenario of a window rupture. As described in the previous section, two ZnSe laser windows were integrated into a tee assembly that was pressurized to 1.1 bar absolute pressure, and the pressure was monitored by the instrument control software. In the scenario that one of the windows failed, the pressure would drop to ambient (1 bar), and the control software was designed to immediately shut off the heating laser, to prevent failure of the second window.

A HEPA filter on the gas cross purge and an in-line filter on the vacuum chuck prevented any sample from leaving the containment vessel.

PuO_{2-x} samples were prepared in a separate laboratory fully equipped and certified for radiological work. All activities performed with radioactive materials followed Argonne National Laboratory's Environment, Safety and Health policies. Preparation of the PuO_{2-x} samples, including uniaxial pressing, sintering, and air milling, was performed in a negative-pressure radiological glovebox. The glovebox was equipped with an attached induction furnace that enabled sintering the pressed pellets in the same glovebox. The glovebox circulation lines, the induction furnace vacuum line, and the exhaust line for the air milling process were equipped with HEPA filters to mitigate the release of PuO_{2-x} particulates outside of the glovebox.

The resulting spheroid pellets were transferred to a radiological fume hood. The spheroid pellets did not contain loose particulates, enabling handling in the fume hood. The three samples were loaded into the radioactive-containment sample holder (item (11) in Supplementary Fig. 1) within the fume hood. The sample holder included primary and secondary enclosures to ensure the pellets were not released. The holder was surveyed for loose radioactive contamination before being transferred from the radiological fume hood into a clean radiological benchtop contamination area. The sample holder was then loaded into the sample containment antechamber (item (2) in Supplementary Fig. 1) of the levitation instrument, and the device was sealed. A radiological contamination survey of the hermetically sealed levitation instrument revealed no external contamination.

The sealed aerodynamic levitation instrument was loaded into a DOT Type A 85-gal drum for transfer to the Advanced Photon Source, where it was installed at the 6-ID-D beamline. After the

levitation tests were performed, the levitation instrument was repackaged and transferred back to the radiological laboratory where the samples were initially prepared. The entire apparatus was placed into a radiological standing hood, where the hermetical seal was broken so the radioactive-containment sample holder could be removed from the antechamber. The sample holder was returned to the radiological fume hood and the pellets were removed and packaged for long term storage. The aerodynamic levitation instrument including sample holder was resealed and transferred into the DOT Type A 85-gal drum for disposal.

IV. Aerodynamic levitation of samples

PuO_{2-x} samples heated under 5% CO (Ar balance), Ar, or 1% O_2 (Ar balance) lost 46-50% of their mass during levitation experiments due to volatilization. Most of this mass loss occurred above 2200 K, and molten samples were held isothermally for no more than 1 min. Below 2200 K, solid samples were held isothermally for 1-2 min during each X-ray diffraction measurement, with minimal volatilization based on visual observation. Volatilization was much more severe during heating under 100% O_2, such that the sample could not be fully melted. The sample recovered after heating in 100% O_2 had a fluffy, cauliflower-like appearance with regions black, tan, and green in color. Volatilization was also severe for CeO_{2-x} with all levitation gases, so rapid heating was employed with an isothermal hold of only 10 s for X-ray measurements of the melt.

V. Temperature uncertainty

For sample temperature measurements, two sources of uncertainty are considered. The largest source of uncertainty, specific to solid samples, arises from the small spot size of the focused heating laser beam and sluggish heat transfer within the sample. These result in significant thermal gradients across the sample and, consequently, noise in the pyrometer readings as the sample moves: during isothermal periods, the standard deviation of temperature measurements was between 70 and 110 K. An exemplary pyrometer trace for a solid sample is shown in Extended Data Fig. 3a-b. Temperature gradients for this aerodynamic levitation and laser heating instrument have been shown to be as large as 180 to 310 K across the top region of solid samples, through which the X-ray beam passes. Temperature is much more uniform once the sample melts, typically achieving temperature gradients of 10 to 30 K across the top of the sample[4]. Extended Data Fig. 3c shows the temperature of a molten sample during the short period for which X-ray measurements were analyzed.

The second source of temperature uncertainty arises from the sample's emissivity, which is not known exactly. For the single-wavelength pyrometer employed in this study (λ = 0.9 μm), the directional spectral emissivity should be used to correct the apparent temperatures measured. First-principles calculations for PuO_2 optical properties have predicted normal spectral emissivities of 0.81 according to Shi *et al.*[5] or 0.96 according to Singh *et al.*[6], for λ = 0.9 μm. These predictions were for stoichiometric PuO_2 near ambient temperatures, so the emissivity for high-temperature solids and the molten state may be different. In the experimental measurements of PuO_2 melting point by de Bruycker *et al.*[7], spectropyrometer measurements showed a normal spectral emissivity of 0.83 ± 0.05 for the solid near its melting point, and the emissivity was nearly independent of wavelength over 0.55-0.92 μm. This result is in good agreement with Shi *et al.*[5] and suggests that the emissivity may not change dramatically with temperature for the solid phase. For this reason, the pyrometry on solid samples in this study have been corrected using a normal spectral emissivity of 0.83. Corrections were also applied for Fresnel reflections from the two silica windows: one on the levitation chamber, and the pyrometer lens.

The emissivity of the melt is expected to be higher than for the solid, partly due to the surface roughness of solids that is not present for the liquid. Unfortunately, emissivity data on molten oxides are scarce and not available for PuO_{2-x}. Molten alumina has a normal spectral emissivity near 0.92[8], and a variety of niobates, titanates, and aluminate melts were found to have emissivities ranging 0.9-0.95[9]. Based on these, a value of 0.92 was used for the normal spectral emissivity of the melts in this study (both PuO_{2-x} and CeO_{2-x}). An uncertainty of ± 0.04 in emissivity results in a maximum temperature uncertainty of ± 50 K, near 3000 K.

While normal spectral emissivities were used for the temperature corrections, the incidence angle of the pyrometer axis with the sample was not necessarily normal. As shown in Fig. 1a, the pyrometer axis was inclined at a 45° angle relative to the vertical. The pyrometer was aligned near the top of the sample, slightly to the side nearest the pyrometer. This geometry results in an incidence angle that deviates by <45° from the normal. Insulators are generally Lambertian (i.e., their directional emissivity is independent of incidence angle) up to ~40° away from normal[10]. Because this Lambertian behavior has been observed broadly in oxides (including alumina),

fluorides, and carbides, we assume that the spectral directional emissivity for our samples at the measured incidence angle is not significantly different from the normal values.

In summary, we estimate the temperature uncertainty to be ± 150 K in solid samples, due to spatial temperature variations, and ± 50 K in liquid samples, due to emissivity uncertainty.

A final consideration is that the pyrometer window may have received deposits of volatilized sample, which would result in lowering of the window transparency as experiments were performed (i.e., a lower effective emissivity for the temperature correction than we have implemented). Visual observation of the window after the experiments did not reveal noticeable changes in window transparency. (Due to radiological safety procedures, the windows could not be removed for cleaning between heating runs.)

VI. Sample compositions and uncertainty

Models relating composition and oxygen gas partial pressure

Sample compositions were calculated using the measured temperature, the oxygen partial pressure of the process gas (pO_2), and a model for the composition-pO_2 relationship in hypostoichiometric *f*-PuO_{2-x}. Several models are available in the literature, including one by Besmann and Lindemer[11] with two slightly revised, subsequent versions[12,13], a model by Kato *et al.*[14], and the phase diagrams developed by Guéneau *et al.*[15–17]. Each of these models was considered for use in estimating the sample compositions. Ultimately, we decided to use the original Besmann and Lindemer model[11]. Below we describe and compare the different models and their variations, and we provide our reasoning for this selection.

Besmann and Lindemer's original model[11] used a thermodynamic analysis for a mixture of PuO_2 and $Pu_{4/3}O_2$. The enthalpies and entropies of their thermodynamic equations were fit to the available literature data (4 fitting parameters in total), gathered from 8 different research reports contributed from several different laboratories. This model showed "good agreement…over the entire compositional range"[11] of the data, and uncertainties were provided for the 4 fitting parameters based on a 95% confidence interval. The data used for fitting covered 953-2050 K and O/Pu ratios of 1.67-2.00. This model is hereafter referred to as "BL1985." In subsequent reports by Besmann and Lindemer, this model was revised slightly. The first revision ("BL1986")[12] was to change the mixture equations to better match experimental data on the miscibility gap in *f*-PuO_{2-x} below 1000 K. In the second revision ("B1987")[13], one of the fitting parameters was changed to better accommodate newly collected data at 1400-1610K "by a visual fit to the data by trial and error adjustment of the parameters"[13].

The model by Kato *et al.*[14] follows the approach by Komeno *et al.*[18]. Both reports construct equilibria expressions for defects in *f*-PuO_{2-x}, and 4-6 parameters were fitted to thermogravimetric data that they collected over 1473-1873 K and O/Pu ratios of 1.84-2.00. No uncertainties were provided for the fitted parameters.

Guéneau *et al.* conducted an exhaustive, critical analysis of the prior thermodynamic data and analyses on the Pu-O system, from which an updated Pu-O phase diagram was calculated using the CALPHAD approach[15]. This phase diagram was updated[16] to account for the reassessed melting point of PuO_2[19] and later adjusted slightly[17]. Specific information on composition-pO_2 relationships for *f*-PuO_{2-x} was provided only in the first version of the model[15].

These different models lead to different estimations for the melt compositions in the current study (Supplementary Table 4), so a critical comparison is necessary. Supplementary Figure 2 compares the Pu-O phase diagram with oxygen partial pressure isobars from each of the models, and Supplementary Table 4 lists the corresponding melt compositions calculated. From a practical standpoint, the reports by Guéneau *et al.* did not provide mathematical expressions to directly relate composition, pO_2, and temperature, so we were unable to calculate melt compositions. For qualitative comparison, Supplementary Fig. 2e provides discrete points gleaned from Guéneau *et al.*[15].

Supplementary Table 4. Melt compositions estimated using different oxidation models. Values for O/Pu, with the range of uncertainty given in parentheses, where available from the models. Models are described in the Supplementary Text section on sample compositions.

Process Gas	BL1985[11]	BL1986[12]	B1987[13]	Kato *et al.*[14]
1% O_2	1.76 (1.74-1.79)	1.84 (1.71-1.96)	1.90 (1.75-1.96)	1.86
Ar	1.69 (1.68-1.71)	1.65 (1.60-1.72)	1.67 (1.61-1.73)	1.71
5% CO	1.57 (1.55-1.58)	1.50	1.50	1.50

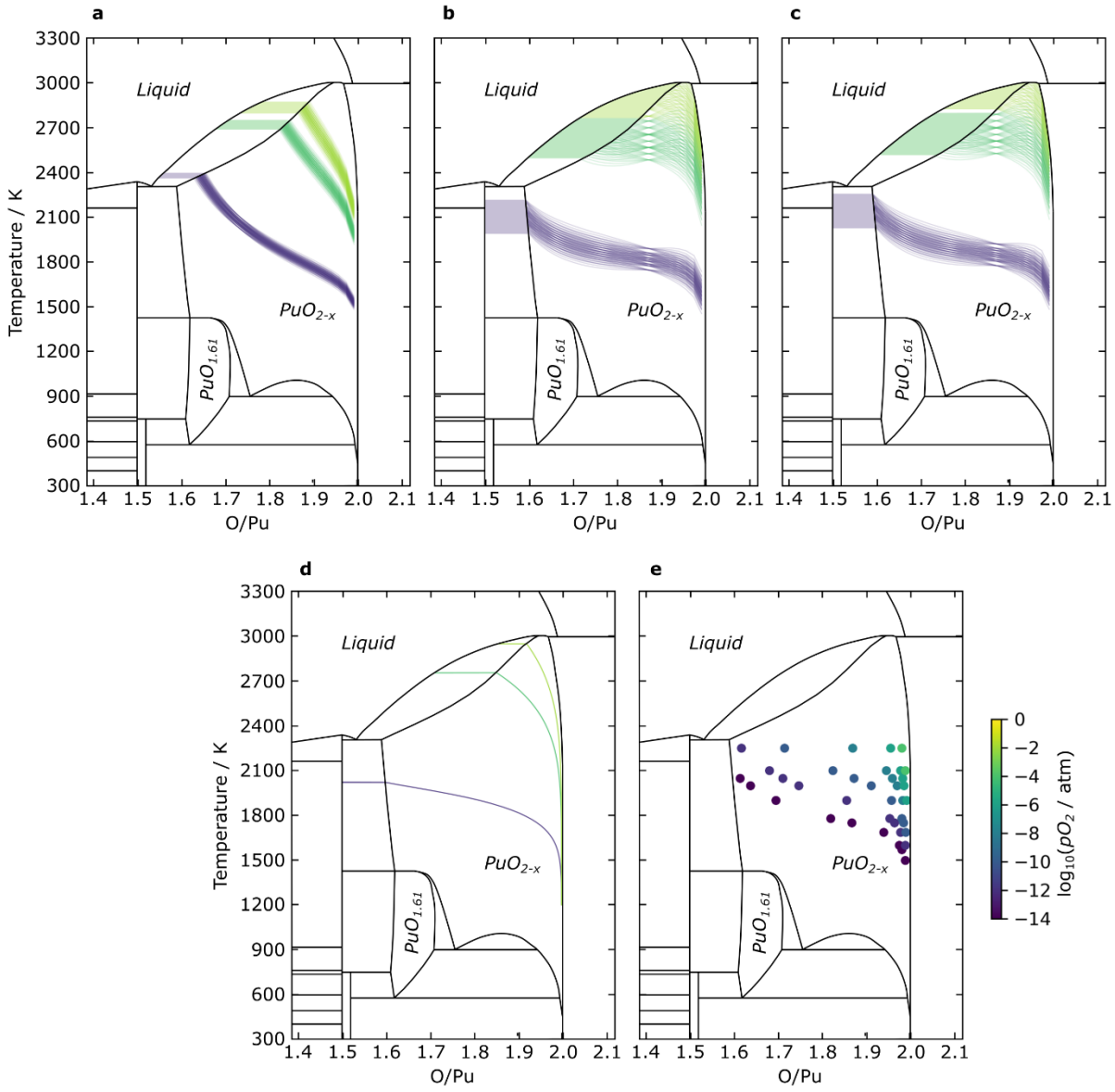

Supplementary Fig. 2. Phase diagram comparison of different oxidation models. Oxygen isobars for $\log_{10}(pO_2)$ = -2, -4, and -12 and their reported uncertainties are shown from **a,** BL1985[11]; **b,** BL1986[12]; **c,** B1987[13]; **d,** Kato *et al.*[14]. For **e,** Guéneau *et al.*[15], discrete points at varying pO_2 are provided. Models are described in the SI section on sample compositions.

Comparing BL1985 with its revised versions BL1986 and B1987 (Supplementary Fig. 2a-c), it is notable that modest changes in the model parameters result in large differences in the melt compositions. This is partly due to the fact that the model must be extrapolated to the solidus, located hundreds of Kelvin higher than the data from which they were fit. Another important difference between BL1985 and its revisions is the uncertainty reported for the model parameters: BL1986 and B1987 both exhibit much larger uncertainty at the solidus, which might be caused by the adjustment in BL1986 that was necessary to reproduce the miscibility gap below 1000 K. For example, the melt processed in 1% O_2 gas has an estimated O/Pu ratio of 1.74-1.79 for BL1985, contrasted with 1.71-1.96 for BL1986 or 1.75-1.96 for B1987. As already mentioned, BL1986 used a specific adjustment to account for the miscibility gap below 1000 K, which is well below the relevant temperature range for the present work. B1987 was adjusted "by trial and error" to accommodate new data from a single laboratory at moderate temperatures (1400-1610 K). Both of these modifications imply that BL1986 and B1987 were optimized for aspects of the low and moderate temperature ranges, and the uncertainties in the fitted parameters were larger. Because BL1985 was not adjusted for these features, its fitting more heavily weighted the high temperature data (up to 2050 K) that is most relevant to the current study.

The model by Kato *et al.* was fitted to only one set of data (first reported in Komeno *et al.*) and did not include the historical data (aside from a comparison, after fitting). Confidence intervals were not reported, which make it difficult to assess the uncertainty. Because BL1985 used data from 8 different reports encompassing larger temperature and compositional ranges, and because it reports the model uncertainty, we selected it for calculating melt compositions. Additionally, only BL1985 predicts direct melting from *f*-PuO_{2-x} for heating under 5% CO gas, which is what we observed here. BL1986, B1987, and the Kato *et al.* models predict conversion to α-Pu_2O_3 prior to melting under 5% CO, but our Rietveld refinements did not indicate the presence of α-Pu_2O_3 (above 1530 K).

The BL1985 model uncertainty results in melt O/Pu uncertainties of ± 0.03, which are the values reported in the main text. The BL1985 melt compositions are within the range of uncertainty for compositions calculated with either the BL1986 or B1987 models (Supplementary Table 4).

After the completion of this study but before its publication, an updated phase diagram was published by Fouquet-Metivier *et al.*[20], which is more recent than the one used in Fig. 1c (by Guéneau *et al.*[16]). If the more recent diagram is used, the melt composition estimates change slightly, yielding O/Pu ratios of 1.77, 1.64, and 1.55 for the gases used here of 1% O_2 (Ar balance), Ar, and 5% CO (Ar balance). These changes are within or near the uncertainty of ± 0.03, relative to the values of 1.76, 1.69, and 1.57 that were used for all analyses and modeling in this study.

Sample-gas equilibration

Sample compositions were calculated using the composition-pO_2 relationships for PuO_{2-x}[11] (Fig. 1c) and CeO_{2-x}[21] (Extended Data Fig. 2), assuming full equilibration of the X-ray probed region with the levitation gas. This region is small (0.2 × 0.5 mm beam cross-section) and aligned with the heating laser beam. The composition-pO_2 relationships are valid for the fluorite phases up to the solidus, at which point the sample reduces as it traverses the solidus-liquidus region along pO_2 isobars in the phase diagram. Because oxygen activity is not known for the liquids, the melt compositions are assigned the values at the liquidus.

The assumption of sample-gas equilibration for estimating PuO_{2-x} composition is supported by three reasons. First, equilibration was observed in prior studies of levitated Fe-bearing silicate melts with X-ray absorption near-edge structure spectroscopy[22,23], using similarly short levitation processing times. Second, for X-ray diffraction of solid samples, several consecutive 30 s measurements were collected at each temperature. The first scan at each temperature was not used in the final analysis, and the latter measurements were reproducible. Third, the composition of samples recovered after melting were consistent with the sample-gas equilibration assumption. For example, the recovered PuO_{2-x} sample after melting under 5% CO (Ar balance) contained a mixture of an FCC phase with lattice parameter $a = 5.496(1)$ Å and a BCC phase with $a = 10.995(1)$ Å. These lattice parameters are outside the ranges expected for equilibrium phases of *f*-PuO_{2-x} and α-Pu_2O_3 at room temperature, suggesting they are metastable quenched products. Gardner *et al.*[24] reported lattice parameter data for Pu-O samples of varying O/Pu ratio up to 1273 K, which contained mixtures of BCC α-Pu_2O_3, BCC "$PuO_{1.61}$", and FCC *f*-PuO_{2-x}. Extrapolation of those data at 973-1273 K to room temperature suggests the recovered sample here is a mixture of quenched "$PuO_{1.61}$" and *f*-PuO_{2-x}. The fractions of these two phases yield a mean composition of $PuO_{1.66}$, which matches almost identically the solidus composition expected for full gas equilibration ($PuO_{1.65}$). This provides evidence that the heated region of the sample did indeed equilibrate with the surrounding gas during heating, specifically within the 1-2 min spent at each isotherm. The liquid is expected to equilibrate even faster. Upon turning off the laser, the liquid likely oxidized rapidly to the solidus composition ($PuO_{1.65}$), after which the solid did not change composition significantly during the few seconds needed for complete cooling.

For heating under 5% CO (Ar balance), the unknown levels of gas impurities introduce uncertainty in pO_2 at high temperatures, resulting in compositional uncertainty. Calculations of pO_2 assumed up to 3 ppm CO_2, per the gas supplier's specification. The corresponding PuO_{2-x} compositions had O/Pu ratios 0.03-0.06 higher than that suggested by extrapolation of prior chemical expansion data[24]. This discrepancy in composition corresponds to a gas impurity of 0.4-1.0 ppm CO_2, which is reasonable given the gas supplier's maximum limit of 3 ppm. For the analyses in this study, all compositions are those calculated assuming 3 ppm CO_2 in the 5% CO gas, since the approach relying on prior chemical expansion data is also prone to uncertainty, as it requires extrapolating data in the 973-1273 K range to nearly 2500 K.

Prior to heating each sample, the levitation chamber was flushed with the process gas for at least 30 min to ensure that the surrounding gas composition was the same as the levitation gas.

One recovered sample that was observed to contact the nozzle while it was molten was checked for Al contamination using ICP mass spectrometry. Contamination was found to be negligible at 424 ppm.

VII. X-ray total scattering analyses

Rietveld refinements

X-ray diffraction patterns were compared against fluorite PuO_2 (*f*-PuO_2), α-Pu_2O_3, β-Pu_2O_3, PuO, and all phases of metallic Pu (α, β, γ, δ, δ', and ε). No Bragg peaks were observed for metallic Pu in any sample, before or after melting, in any gas condition used here. The initial Pu-O material contained a mixture of *f*-PuO_{2-x}, α-Pu_2O_3, β-Pu_2O_3 (Extended Data Fig. 5a) and upon heating transformed to purely *f*-PuO_{2-x}. The sample quenched after heating in 5% CO (Ar balance) contained a mixture of *f*-PuO_{2-x} and "$PuO_{1.61}$," which is a high-temperature structural variant of α-Pu_2O_3 with a different lattice parameter[24]. The sample recovered after heating in 100% O_2 (without melting) was pure *f*-PuO_2 with a = 5.397(1) Å (Extended Data Fig. 5b), matching prior measurements of a = 5.396 Å[24].

Supplementary Figure 3 shows the lattice parameter for the fluorite phase of the PuO_{2-x} sample heated under 5% CO (Ar balance). These data are the same as those used in Fig. 2, which shows atomic number density vs. temperature. By plotting lattice parameter, the arrest in lattice expansion above 1800 K is more clearly evident than in the density data, since the density continues to decrease slowly above 1800 K due to chemical reduction (i.e., making the number of atoms per unit cell decrease). Lattice parameter uncertainties from the Rietveld refinements were largest at higher temperatures but no greater than ± 0.004 Å.

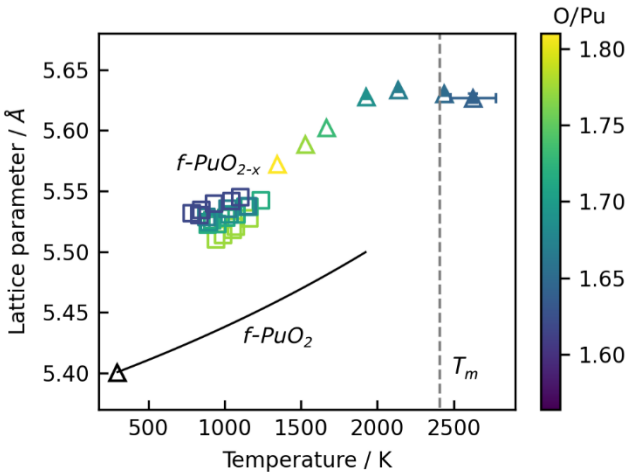

Supplementary Fig. 3. Lattice parameter of *f*-PuO_{2-x} during heating. Sample heated under 5% CO (Ar balance), with triangle markers' colors corresponding to the O/Pu ratio given by the pO_2 isobars in Fig. 1c. Triangle markers are unfilled for solid samples and half-filled for solid/liquid mixtures. Representative error bars are shown for the highest temperature measurement. Thermal expansion for stoichiometric *f*-PuO_2 (black curve)[25] and chemical expansion for *f*-PuO_{2-x} (colored squares)[24] up to the maximum temperatures previously reported.

Melt densities

The density ratio of *f*-PuO_{2-x} to stoichiometric *f*-PuO_2 was calculated for compositions ranging $PuO_{1.87}$ to $PuO_{1.62}$ using X-ray diffraction data at 973 K[24]. The melt density for stoichiometric PuO_2, simulated by molecular dynamics[26], was then scaled by the density ratio to obtain estimates for melt compositions of $PuO_{1.76}$, $PuO_{1.69}$, and $PuO_{1.57}$: 0.0561, 0.0548, and 0.0551 atoms $Å^{-3}$. The density was then refined from the X-ray PDF by minimizing $|\int rT(r)dr|$ over the real-space distance range below any atomic pair correlations, r < 1.6 Å. The refined density values were 0.0571, 0.0572, and 0.0559 atoms $Å^{-3}$, which are 1.5-4.4% higher than the initial estimates. For Fig. 2b, the liquid density is plotted with an error bar of ± 2.5%.

For CeO_{2-x}, the fluorite solid density for $CeO_{1.75}$ at the solidus was calculated as 6.57 g cm^{-3}, based on thermal and chemical expansion effects[27]. The relative volume increase upon melting was assumed to the be same as La_2O_3 and Nd_2O_3, 15.7%[28], yielding a melt density estimate of 5.54 g cm^{-3} (0.0546 atoms $Å^{-3}$). This is slightly larger than the average of liquid La_2O_3 and Nd_2O_3 densities[28], 5.39 g cm^{-3}, which is consistent with the CeO_{2-x} solid's trend of increasing density as composition moves from Ce_2O_3 to CeO_2. The PDF-refined density for $CeO_{1.75}$ was 0.0575 atoms $Å^{-3}$, 5.3% higher than the initial estimate and in close agreement with $PuO_{1.76}$.

Interpretation of Bragg and diffuse scattering in PuO_{2-x}

Upon heating, PuO_{2-x} exhibited Bragg and diffuse scattering simultaneously over the temperature range 1930-2630 K. The presence of diffuse scattering indicates a liquid or highly disordered solid phase, which must have been co-present with the crystalline fluorite phase. A mixture of solid and liquid would be expected when the material is between the solidus and liquidus of the phase diagram, but this mixture of scattering was observed over a much broader temperature range and began ~470 K below the solidus. This raises the possibility of a high-temperature, highly disordered solid phase suggestive of a Bredig transition[29], as has been evidenced for UO_{2-x}[2,30,31]. However, Bredig transitions in fluorite oxides are associated with disordering of the oxygen sublattice, and since the X-ray scattering is predominantly due to Pu (W_{OO} = 1.4% at Q = 0 $Å^{-1}$), it is unlikely that such disorder would manifest in the total X-ray structure factors[2].

Another possible explanation is that the X-ray beam was probing regions of solid and liquid simultaneously, which can result from a small laser spot size on the sample. To interrogate this hypothesis, aerodynamic levitation and laser beam heating were conducted on $75La_2O_3$-25CaO (LC) samples, which have a solidus-liquidus gap similar to PuO_{2-x}. The temperature and X-ray scattering behavior of LC samples qualitatively matched those of PuO_{2-x}: simultaneous Bragg and diffuse scattering were observed as low as ~1800 K, ~500 K below the solidus. The heating laser focus was then adjusted to create a larger spot size on the sample, which should decrease the magnitude of spatial temperature variations in the sample. Measurements were repeated with the less-focused laser, and the mixed Bragg and diffuse scattering did not appear until ~2100 K. These observations suggest that the mixed scattering observed in high-temperature PuO_{2-x} arose from a simple solid/liquid mixture, and thus these measurements cannot inform on the possible existence of a Bredig transition.

The X-ray scattering intensity over 1930-2730 K was fitted with a simple two-state mixture model, using the 1930 K data as the *f*-PuO_{2-x} endmember and the 2730 K data as the liquid

endmember. This model provides approximate values for the fraction of *f*-PuO_{2-x} present: ~5% at 2140 K and ~2% at 2440 K.

Pair distribution function (PDF) analysis

During data reduction to obtain the X-ray structure factors, the top hat convolution[32] in GudrunX was applied to remove residual long-wavelength background in *S(Q)* that occurs due to imperfect corrections to the data. Due to the very large X-ray absorption of Pu, the data corrections for sample absorption and multiple scattering are likely the reasons here that *S(Q)* is not on a flat baseline at high-*Q* prior to applying the top hat convolution. The top hat convolution helps flatten the *S(Q)* baseline at high-*Q*, which dampens oscillations in the low-*r* region of the PDF at real-space distances shorter than any atomic correlations. Extended Data Fig. 7 compares the structure factors and total PDFs processed with vs. without the top hat convolution. All analyses in this study use structure factors with the top hat convolution applied.

The first few peaks of the $PuO_{1.76}$ total PDF were fit using Gaussian distributions in NXFit[33]. Extended Data Fig. 1a shows the result when two distributions were used to fit only the leading edges of the first and second peaks. These correspond primarily to the PuO and PuPu partials. The difference (Extended Data Fig. 1a, dashed green) between the X-ray PDF and fitted distributions shows a peak near 2.8 Å, suggesting the presence of longer PuO bonds than can be modeled with a single Gaussian distribution. This motivated the use of two separate PuO distributions for the first peak (Extended Data Fig. 1b). Next, Gaussian distributions were added for the first two OO coordination shells near 2.70 and 3.82 Å and the second PuO shell near 4.48 Å, based on the corresponding distances in crystalline *f*-PuO_2. The fitting parameters were then iteratively refined subject to constraints that ensured the model remained realistic in comparison to crystalline *f*-PuO_2 and α-Pu_2O_3. The OO peaks contribute little to the total PDF and quantitative fitting of the second PuO peak has substantial uncertainty, but they were included in the overall fitting procedure to obtain the most robust estimates for the first PuO coordination shell (i.e., the Gaussian distributions near 2.23 and 2.68 Å).

It is important to note that the two distinct PuO distributions that were fit to the first peak do not directly correspond to Pu(III)-O and Pu(IV)-O correlations, since this is purely an empirical fitting procedure. However, the necessity of having two PuO distributions to adequately fit the first peak motivated the definition of separate Pu(III) and Pu(IV) species in the initial setup for the EPSR model.

VIII. Empirical potential structure refinement

Several models were simulated to check their sensitivity to temperature and composition. For temperatures of 3000 ± 500 K, the model exhibited only subtle changes. For O/Pu ratios, variations of up to ± 0.09 away from O/Pu = 1.76 resulted in worse agreement of the model's Pu-O peak with the X-ray PDF. An alternative model was also simulated with a single Pu cation specie, with charge corresponding to the weighted average of Pu(III) and Pu(IV) species in the main model. This corresponds to the case in which electron transfer between Pu(III)-Pu(IV) cation pairs occurs on a timescale much shorter than that for structural relaxation. However, the model containing a single Pu cation specie exhibited a much narrower Pu-O distribution than observed in the X-ray PDF. The Pu-O mean coordination number varied by 0.4 between the models with one vs. two cation species, so ± 0.4 is reported as the uncertainty in the main text.

The insensitivity of the EPSR refinement to model temperature over the 2500-3500 K range is important because $PuO_{1.76}$ and $CeO_{1.75}$ were measured experimentally at different temperatures within this range: 3000 K for $PuO_{1.76}$, ~150 K above its liquidus, and 2580 K for $CeO_{1.75}$, very near its liquidus of 2566 K (Extended Data Fig. 2).

References for Supplementary Information

1. Weber, J. K. R. *et al.* Aerodynamic levitator for in situ x-ray structure measurements on high temperature and molten nuclear fuel materials. *Rev. Sci. Instrum.* **87**, 073902 (2016).
2. Skinner, L. B. *et al.* Molten uranium dioxide structure and dynamics. *Science* **346**, 984–987 (2014).
3. Benmore, C. J. *et al.* Laser heating of polycrystalline nuclear materials. *AIP Conf. Proc.* **2054**, 40015 (2019).
4. McCormack, S. J., Tamalonis, A., Weber, R. J. K. & Kriven, W. M. Temperature gradients for thermophysical and thermochemical property measurements to 3000 °C for an aerodynamically levitated spheroid. *Rev. Sci. Instrum.* **90**, 15109 (2019).
5. Shi, H., Chu, M. & Zhang, P. Optical properties of UO2 and PuO2. *J. Nucl. Mater.* **400**, 151–156 (2010).
6. Singh, S. *et al.* Ab-initio calculation on electronic and optical properties of ThO2, UO2 and PuO2. *J. Nucl. Mater.* **511**, 128–133 (2018).
7. De Bruycker, F. *et al.* The melting behaviour of plutonium dioxide: A laser-heating study. *J. Nucl. Mater.* **416**, 166–172 (2011).
8. Krishnan, S., Weber, J. K. R., Schiffman, R. A., Nordine, P. C. & Reed, R. A. Refractive Index of Liquid Aluminum Oxide at 0.6328 μm. *J. Am. Ceram. Soc.* **74**, 881–883 (1991).
9. Nason, D. O., Yen, C. T. & Tiller, W. A. Measurements of optical properties of some molten oxides. *J. Cryst. Growth* **106**, 221–226 (1990).
10. Bentley, R. E. *Handbook of Temperature Measurement*. (Springer Verlag, 1998).
11. Besmann, T. M. & Lindemer, T. B. Chemical thermodynamic representations of <PuO2-x> and <U1-zPuzOw>. *J. Nucl. Mater.* **130**, 489–504 (1985).
12. Besmann, T. M. & Lindemer, T. B. Improvement in the chemical thermodynamic representation of <PuO2-x> and <U1-zPuzOw>. *J. Nucl. Mater.* **137**, 292–293 (1986).
13. Besmann, T. M. Phase equilibria and thermodynamics of the Pu-O system: 1400 K to 1610 K. *J. Nucl. Mater.* **144**, 141–150 (1987).
14. Kato, M., Nakamura, H., Watanabe, M., Matsumoto, T. & Machida, M. Defect chemistry and basic properties of non-stoichiometric PuO2. *Defect Diffus. Forum* **375**, 57–70 (2017).
15. Guéneau, C., Chatillon, C. & Sundman, B. Thermodynamic modelling of the plutonium-oxygen system. *J. Nucl. Mater.* **378**, 257–272 (2008).
16. Guéneau, C. *et al.* Thermodynamic modelling of advanced oxide and carbide nuclear fuels: Description of the U-Pu-O-C systems. *J. Nucl. Mater.* **419**, 145–167 (2011).
17. Guéneau, C., Chartier, A., Fossati, P., Van Brutzel, L. & Martin, P. Thermodynamic and Thermophysical Properties of the Actinide Oxides. in *Comprehensive Nuclear Materials 2nd edition* 111–154 (Elsevier, 2020).
18. Komeno, A., Kato, M., Hirooka, S. & Sunaoshi, T. Oxygen potentials of PuO2-x. *Mater. Res. Soc. Symp. Proc.* **1444**, 85–89 (2012).
19. De Bruycker, F. *et al.* Reassessing the melting temperature of PuO2. *Mater. Today* **13**, 52–55 (2010).
20. Fouquet-Métivier, P. *et al.* Investigation of the solid/liquid phase transitions in the U–Pu–O system. *Calphad* **80**, 102523 (2023).
21. Zinkevich, M., Djurovic, D. & Aldinger, F. Thermodynamic modelling of the cerium-oxygen system. *Solid State Ionics* **177**, 989–1001 (2006).

22. Alderman, O. L. G. *et al.* Local structural variation with oxygen fugacity in Fe2SiO4+x fayalitic iron silicate melts. *Geochim. Cosmochim. Acta* **203**, 15–36 (2017).
23. Alderman, O. L. G. *et al.* Iron K-edge X-ray absorption near-edge structure spectroscopy of aerodynamically levitated silicate melts and glasses. *Chem. Geol.* **453**, 169–185 (2017).
24. Gardner, E. R., Markin, T. L. & Street, R. S. The plutonium-oxygen phase diagram. *J. Inorg. Nucl. Chem.* **27**, 541–551 (1965).
25. Uchida, T., Sunaoshi, T., Konashi, K. & Kato, M. Thermal expansion of PuO2. *J. Nucl. Mater.* **452**, 281–284 (2014).
26. Ghosh, P. S. *et al.* Melting behavior of (Th,U)O2 and (Th,Pu)O2 mixed oxides. *J. Nucl. Mater.* **479**, 112–122 (2016).
27. Bishop, S. R. *et al.* Chemical Expansion : Implications for Electrochemical Energy Storage and Conversion Devices. *Annu. Rev.* **44**, 205–239 (2014).
28. Granier, B. & Heurtault, S. Density of Liquid Rare-Earth Sesquioxides. *J. Am. Ceram. Soc.* **71**, 466–468 (1988).
29. Günay, S. D., Akgenç, B. & Taşseven. Modeling Superionic Behavior of Plutonium Dioxide. *High Temp. Mater. Process.* **35**, 999–1004 (2016).
30. Ralph, J. Specific Heat of UO2, ThO2, PuO2 and the Mixed Oxides (ThxO1-x)O2 and (Pu0.2U0.8)O1.97 by Enthalpy Data Analysis. *J. Chem. Soc., Faraday Trans. 2* **83**, 1253–1262 (1987).
31. Kurosaki, K. *et al.* Molecular dynamics study of mixed oxide fuel. *J. Nucl. Mater.* **294**, 160–167 (2001).
32. Soper, A. K. Inelasticity corrections for time-of-flight and fixed wavelength neutron diffraction experiments. *Mol. Phys.* **107**, 1667–1684 (2009).
33. Pickup, D., Moss, R. & Newport, R. NXFit: A program for simultaneously fitting X-ray and neutron diffraction pair-distribution functions to provide optimized structural parameters. *J. Appl. Crystallogr.* **47**, 1790–1796 (2014).